Mon. Not. R. Astron. Soc. **323**, 343–361 (2001)

ISO LWS observations of planetary nebula fine-structure lines

X.-W. Liu,[1★] M. J. Barlow,[1] M. Cohen,[2] I. J. Danziger,[3] S.-G. Luo,[4] J. P. Baluteau,[5] P. Cox,[6] R. J. Emery,[7] T. Lim[7] and D. Péquignot[8]

[1]*Department of Physics and Astronomy, University College London, Gower Street, London WC1E 6BT*
[2]*Radio Astronomy Laboratory, 601 Campbell Hall, University of California, Berkeley, CA 94720, USA*
[3]*Osservatorio Astronomico di Trieste, Via G. B. Tiepolo 11, I-34131 Trieste, Italy*
[4]*Beijing Joint Astrophysics Centre, Beijing University, Zhong Guang Cun, Beijing 100871, P. R. China*
[5]*Laboratoire d'Astronomie Spatiale, CNRS, BP 8, F-13376, Marseille Cedex 12, France*
[6]*Institut d'Astrophysique Spatiale, Bât. 120, Université Paris XI, 91405 Orsay, France*
[7]*Space Science Department, Rutherford Appleton Laboratory, Chilton, Oxon OX11 0QX*
[8]*Observatoire de Paris–Meudon, F-92190 Meudon, France*

Accepted 2000 October 25. Received 2000 October 18; in original form 2000 July 10

ABSTRACT

We have obtained 43–198 μm far-infrared (IR) spectra for a sample of 51 Galactic planetary nebulae (PN) and protoplanetary nebulae (PPN), using the Long Wavelength Spectrometer (LWS) on board the *Infrared Space Observatory* (*ISO*). Spectra were also obtained of the former PN candidate Lo 14. The spectra yield fluxes for the fine-structure lines [N II] 122 μm, [N III] 57 μm and [O III] 52 and 88 μm emitted in the ionized regions and the [O I] 63- and 146-μm and [C II] 158-μm lines from the photodissociation regions (PDRs), which have been used to determine electron densities and ionic abundances for the ionized regions and densities, temperatures and gas masses for the PDRs. The strong [N III] and [O III] emission lines detected in the LWS spectrum taken centred on Lo 14 could be associated with the nearby strong radio and infrared source G 331.5−0.1.

We find that the electron densities yielded by the [O III] 88 μm/52 μm doublet ratio are systematically lower than those derived from the optical [Ar IV] λ4740/λ4711 and [Cl III] λ5537/λ5517 doublet ratios, which have much higher critical densities than the 52- and 88-μm lines, suggesting the presence of density inhomogeneities in the nebulae. Ionic abundances, N^+/H^+, N^{2+}/H^+ and O^{2+}/H^+, as well as the N^{2+}/O^{2+} abundance ratio, which provides a good approximation to the N/O elemental abundance ratio, are derived. Although ionic abundances relative to H^+ deduced from the far-IR fine-structure lines are sensitive to the adopted electron density and the presence of density inhomogeneities, the strong dependence on the nebular physical conditions is largely cancelled out when N^{2+}/O^{2+} is calculated from the 57 μm/(52 μm + 88 μm) flux ratio, owing to the similarity of the critical densities of the lines involved.

The temperatures and densities of the PDRs around 24 PN have been determined from the observed [O I] and [C II] line intensity ratios. Except for a few objects, the deduced temperatures fall between 200 and 500 K, peaking around 250 K. The densities of the PDRs vary from 10^4–10^5 cm^{-3}, reaching 3×10^5 cm^{-3} in some young compact PN. With a derived temperature of 1600 K and a density of 10^5 cm^{-3}, the PDR of NGC 7027 is one of the warmest and at the same time one of the densest amongst the nebulae studied. For most of the PN studied, the [C II]-emitting regions contain only modest amounts of material, with gas masses $\lesssim 0.1\,M_\odot$. Exceptional large PDR masses are found for a few nebulae, including NGC 7027, the bipolar nebulae M2-9 and NGC 6302, the young dense planetary nebulae BD+30°3639, IC 418 and NGC 5315, and the old, probably recombining, nebulae IC 4406 and NGC 6072.

Key words: ISM: abundances – planetary nebulae: general.

★ E-mail: xwl@star.ucl.ac.uk

Table 1. Journal of LWS observations.

Target	RA(2000)	DEC(2000)	Date	AOT	TDT	Exp. (sec)
BD+30 3639	19 34 45.2	30 30 58.8	1996 Nov 6	1	35501412	1479
CPD−56°8032	17 09 00.9	−56 54 48.1	1996 Feb 9	1	08401538	1765
Cn 1-5	18 29 11.6	−31 29 59.7	1997 Mar 15	1	48500404	1961
Cn 1-5 off	18 28 59.8	−31 24 56.7	1997 Mar 15	1	48500405	2121
HD 44179	6 19 58.1	−10 38 13.1	1997 Oct 25	1	70901203	3641
HD 44179 off	6 19 31.0	−10 38 35.0	1997 Oct 25	1	70901204	1381
Hb 12	23 26 14.7	58 10 54.7	1997 Jun 9	1	57101028	1369
Hb 12 off	23 26 40.3	58 13 32.4	1997 Jun 9	1	57101029	1529
He 2-113	14 59 53.5	−54 18 07.7	1996 Feb 4	1	07903229	1605
He 2-113	14 59 53.5	−54 18 07.7	1997 Sep 14	1	66900121	2441
He 2-113 off	15 00 24.7	−54 24 45.8	1996 Feb 4	1	07903253	1765
He 2-131	15 37 11.7	−71 54 53.2	1996 Aug 16	1	27301830	1479
Hu 2-1	18 49 47.4	20 50 39.3	1997 Mar 1	2	47100660	977
IC 3568	12 33 06.6	82 33 49.7	1997 Nov 2	1	71703513	2441
IC 3568	12 33 06.7	82 33 49.8	1996 Jun 17	1	21304921	1469
IC 418	5 27 28.3	−12 41 48.2	1997 Oct 4	1	68900805	3641
IC 418	5 27 28.3	−12 41 48.2	1998 Apr 5	1	86801205	3428
IC 418 off	5 27 07.6	−12 34 45.4	1997 Oct 5	1	68900806	1381
IC 418 off	5 27 07.6	−12 34 45.4	1998 May 5	1	86801206	1328
IC 4191	13 08 48.2	−67 38 32.5	1997 Mar 18	2	48800166	817
IC 4406	14 22 26.5	−44 09 05.9	1997 Feb 5	1	44700327	1529
IC 4634	17 01 33.4	−21 49 33.1	1997 Mar 22	2	49201270	817
IC 4997	20 20 08.7	16 43 53.3	1996 Nov 24	1	37400215	1911
IC 4997 off	20 20 17.2	16 48 45.5	1996 Nov 24	1	37400216	2071
IC 5117	21 32 30.8	44 35 47.3	1996 Nov 18	1	36701822	2071
IRAS 21282+5050	21 29 58.3	51 03 59.8	1996 Oct 28	1	34602320	1319
IRAS 21282+5050 off	21 30 23.4	51 06 02.1	1996 Oct 28	1	34602321	1479
Lo 14	16 11 45.5	−51 17 57.2	1998 Feb 9	1	81700132	2441
Lo 14 off	16 10 38.6	−51 17 32.0	1998 Feb 6	1	81400156	1541
M 1-42	18 11 04.6	−28 59 00.5	1997 Oct 19	1	70302104	2441
M 1-42 off	18 11 04.6	−28 49 00.5	1997 Oct 19	1	70302105	1381
M 1-92	19 36 18.9	29 32 50.1	1996 Nov 18	1	36701902	1319
M 1-92 off	19 36 54.5	29 30 33.3	1996 Nov 18	1	36701942	1479
M 2-55	23 31 51.0	70 22 14.1	1998 Jan 27	1	80401605	1541
M 2-56	23 56 36.5	70 48 13.0	1997 May 29	1	56000431	1369
M 2-56 off	23 55 54.8	70 43 15.2	1997 May 29	1	56000441	1529
M 2-9	17 05 37.8	−10 08 32.4	1996 Feb 10	1	08501036	1765
M 2-36	18 17 41.8	−29 08 19.6	1997 Oct 19	1	70302001	2441
M 2-36 off	18 17 41.8	−29 15 19.6	1997 Oct 19	1	70302002	1381
Mz 3	16 17 13.6	−51 59 06.1	1996 Feb 9	1	08402133	1605
Mz 3 off	16 17 56.9	−52 04 06.7	1996 Feb 9	1	08402156	1765
NGC 40	0 13 00.9	72 31 20.0	1997 Mar 3	1	47300616	1369
NGC 40 off	0 13 18.7	72 39 32.6	1997 Mar 3	1	47300646	1529
NGC 2346	7 09 22.5	−00 48 22.4	1997 Nov 1	1	71602536	2441
NGC 3132	10 07 01.8	−40 26 09.7	1996 Jul 15	1	24200118	1479
NGC 3242	10 24 46.0	−18 38 38.8	1996 Jun 25	1	22200119	1469
NGC 3918	11 50 18.9	−57 10 51.1	1996 Aug 9	1	26700720	1319
NGC 3918 off	11 49 19.1	−57 09 01.4	1996 Aug 9	1	26700749	1479
NGC 5189	13 33 33.4	−65 58 35.0	1996 Sep 29	1	31800124	1319
NGC 5189 off	13 32 47.1	−65 52 26.2	1996 Sep 29	1	31800150	1479
NGC 5315	13 53 57.8	−66 30 51.8	1996 Aug 23	1	28001926	1319
NGC 5315 off	13 55 01.7	−66 37 29.6	1996 Aug 23	1	28001951	1479
NGC 5882	15 16 49.8	−45 38 56.4	1997 Mar 14	2	48400668	709
NGC 6072	16 12 58.8	−36 13 38.6	1996 Sep 9	1	29701631	1319
NGC 6072 off	16 12 30.1	−36 21 56.6	1996 Sep 9	1	29701655	1479
NGC 6153	16 31 30.9	−40 15 22.4	1996 Feb 9	1	08402635	1605
NGC 6153 off	16 31 57.5	−40 21 22.3	1996 Feb 9	1	08402657	1765
NGC 6302	17 13 44.2	−37 06 11.2	1996 Sep 1	1	28901940	1319
NGC 6302 off	17 13 29.3	−37 14 04.6	1996 Sep 1	1	28901960	1479
NGC 6537	18 05 13.3	−19 50 13.7	1997 Feb 28	1	47000802	1369

Table 1 – *continued*

Target	RA(2000)	DEC(2000)	Date	AOT	TDT	Exp. (sec)
NGC 6537	18 05 13.3	−19 50 13.7	1997 Oct 18	1	70300625	2441
NGC 6537 off	18 05 11.1	−19 55 43.6	1997 Feb 28	1	47000833	1529
NGC 6543	17 58 33.3	66 37 58.7	1996 Jul 28	1	25500701	1479
NGC 6567	18 13 44.9	−19 04 19.3	1997 Feb 25	2	46700772	817
NGC 6572	18 12 06.3	06 51 13.6	1996 Sep 21	1	30901603	1319
NGC 6572 off	18 11 40.5	06 54 36.5	1996 Sep 21	1	30901634	1479
NGC 6578	18 16 17.1	−20 26 59.3	1997 Mar 23	2	49301474	745
NGC 6720	18 53 35.7	33 01 40.3	1996 Nov 16	1	36600206	1479
NGC 6741	19 02 36.2	−00 26 47.0	1997 Mar 10	2	48001461	977
NGC 6781	19 18 28.0	06 32 18.5	1997 Mar 29	1	49901108	1369
NGC 6781 off	19 18 25.7	06 26 45.5	1997 Mar 29	1	49901136	1529
NGC 6790	19 22 56.8	01 30 46.6	1997 May 3	2	53400762	977
NGC 6826	19 44 48.2	50 31 30.9	1996 Sep 14	1	30201113	1479
NGC 6884	20 10 23.4	46 27 39.0	1997 May 10	2	54101363	977
NGC 6886	20 12 42.9	19 59 22.4	1997 May 6	2	53701964	977
NGC 7009	21 04 10.8	−11 21 56.6	1996 Oct 25	1	34400517	1479
NGC 7662	23 25 53.9	42 32 05.4	1997 Jun 6	1	56801325	1529
Vy 2-2	19 24 21.9	09 53 54.8	1997 May 16	1	54700310	1369
Vy 2-2 off	19 24 36.8	09 58 25.1	1997 May 16	1	54700311	1529

1 INTRODUCTION

Planetary nebulae (PN) are gaseous envelopes thrown off from low- and intermediate-mass stars in their advanced evolutionary stages. PN are major sources of fresh C, N and s-process heavy elements in the Universe. Because of their particularly simple structures, i.e. a generally symmetric nebula excited by one centrally located star, PN are excellent astrophysical laboratories to study atomic processes relevant to ionized gaseous nebulae. Many PN are surrounded by neutral and/or molecular envelopes. Observations of these objects thus also provide an opportunity to study the physics and chemistry of photodissociation regions (PDRs) and dense molecular material exposed to strong radiation fields in different chemical environments (C- or O-rich).

We have observed several dozen Galactic PN in the far-IR using the Long Wavelength Spectrometer (LWS; Clegg et al. 1996) on board the *Infrared Space Observatory* (*ISO*; Kessler et al. 1996). The spectra cover a wavelength range from 43–197 μm. For many of them, spectra taken with the Short Wavelength Spectrometer (SWS; de Graauw, Haser & Beintema 1996) were also obtained. The targets in our sample were selected for two main scientific purposes. The first was to study the far-IR dust continua and emission features. The objects selected for this purpose are therefore mostly young dense nebulae with strong dust continuum emission, and often have a relatively low excitation class. We have also included a few protoplanetary nebulae (PPN) in our sample, such as the Red Rectangle (HD 44179) and IRAS 21282+5050. PPN are objects which have recently left the asymptotic giant branch (AGB) and their nuclei have not reached a temperature high enough to create an ionized region.

The second scientific goal of our observations was to determine heavy element abundances for PN using the far-IR fine-structure lines. Lines falling within the LWS spectral coverage include [N II] 122 μm, [N III] 57 μm and [O III] 52 and 88 μm. The targets selected for this purpose generally have well-developed ionized regions of high surface brightness and a moderate to high excitation class. Preference was given to those nebulae for which we have already obtained deep, high spectral resolution optical spectra. Many space-borne facilities, including *ISO* and the *International Ultraviolet Explorer* (*IUE*) often use a large entrance aperture and thus yield total line fluxes for the entire nebula, whereas modern ground-based optical spectroscopy generally employs a long-slit spectrograph, sampling only parts of the entire nebula. In order to obtain total fluxes of optical emission lines for the whole nebula, extended nebulae in our sample were observed by uniformly scanning the long-slit of an optical spectrograph across the entire nebular surface. The average spectrum thus obtained, when combined with the total nebular Hβ flux measured with a large aperture, then yields absolute fluxes for all emission lines detected in the optical spectra, which are then directly comparable to line fluxes measured with the *ISO* LWS (entrance aperture ∼70 arcsec) and SWS (aperture from 14×20 arcsec^2 to 20×33 arcsec^2, depending on the observed wavelength bands) in the infrared and those measured previously with *IUE* (aperture 10.3×23 arcsec^2) in the ultraviolet.

One of the most pressing problems in nebular abundance determinations has been that the ionic abundances of heavy elements, such as C, N, O and Ne, relative to H, deduced from optical recombination lines (ORLs) have been found to be systematically higher than those deduced from optical and UV collisionally excited lines (CELs). The discrepancy varies from target to target and covers a wide range of values, from near unity to more than an order of magnitude (e.g. Liu et al. 1999). Given the strong dependence of ionic abundances deduced from optical and UV CELs on the adopted electron temperature and density of the emitting region, the discrepancy has often been attributed to the presence of large temperature fluctuations (Peimbert 1967; 1971) and/or density inhomogeneities (Rubin 1989; Viegas & Clegg 1994). Direct observational evidence in favour of such interpretations still remains to be found however. With excitation energies of $\lesssim 10^3$ K, ionic abundances derived from the IR fine-structure lines are insensitive to nebular electron temperatures and thus provide a direct test of temperature fluctuations as the cause of the discrepancy. Furthermore, infrared fine-structure lines span a wide range of critical densities and can be used to probe nebular density structure, inhomogeneities and their effects on abundance

determinations without complications from temperature or ionization stratification.

Apart from fine-structure lines from ionized regions, the LWS spectra also yield the [O I] 63- and 146-μm and [C II] 158-μm fine-structure line fluxes emitted by the PDRs of some planetary nebulae. The simultaneous detection of these three important PDR cooling lines provides a way to determine directly the PDR temperatures, densities and gas masses.

In this paper, we present fine-structure emission line fluxes for 51 PN and PPN measured by us using the LWS. Results from the SWS spectra will be presented in a future paper. LWS fine-structure line fluxes for a subset of 21 PN in the current sample were previously presented by Liu (1997), derived from spectra processed with Version 6 of the LWS Offline Processing (OLP). The current fluxes are based on the more recent LWS OLP Version 7. In Section 2, we describe the observations and data reduction and present the line fluxes. The electron densities deduced from the [O III] 52 μm/88 μm ratio are presented in Section 3 and compared to those derived from optical observations. The ionic abundances derived from the fine-structure lines are presented in Section 4. The physical properties of nebular PDRs deduced from the [O I] 63- and 146-μm lines and the [C II] 158-μm line are discussed in Section 5. Finally, in Section 6 we present estimates of the nebular neutral region masses derived from the [C II] 158-μm line fluxes.

2 OBSERVATIONS AND DATA REDUCTION

A journal of the LWS observations is given in Table 1. Column 1 gives the usual nebular names. Columns 2 and 3 are the coordinates used for pointing the LWS during the observation, as recorded in the image headers of the data products. Columns 4–7 give the observation date, the AOT (Astronomical Observation Template) number used for the observation, the *ISO* data product number (TDT) and the total exposure time in seconds. The first three digits of the TDT number give the *ISO* orbit number during which the observation was carried out.

Most of our LWS observations were carried out using AOT 1, which yielded full grating scan spectra from 43–197 μm. Each spectrum consists of ten overlapping sub-spectra, one from each of the ten detectors of the LWS. For each target, multiple (usually 6–8) scans were obtained, each with one 0.5-s integrating ramp at each grating position. The spectra were sampled at 1/4 of a spectral resolution element, the latter being 0.29 μm full width half-maximum (FWHM) for detectors SW1–SW5 (43–92 μm) in second spectral order and 0.6 μm FWHM for detectors LW1–LW5 (84–197 μm) in first order. A few nebulae were observed with LWS AOT 2, designed to measure a single line flux by scanning a limited spectral region centred on the line. Three lines were observed, namely [N III] 57 μm and [O III] 52 and 88 μm.

The Galactic plane is a strong emitter of far-IR dust continuum radiation and of the [O I] 63- and 146-μm and [C II] 158-μm fine-structure lines, the latter being major cooling lines in the diffuse interstellar medium (ISM). Prior to the *ISO* observations, all the targets were examined on the online 60- and 100-μm *IRAS* Sky Survey Atlas (Wheelock et al. 1994). For sources embedded in significant Galactic background emission, an identical off-source spectrum representative of the local background emission was also obtained, usually taken a few arcmin away from the source. The offset position was chosen to have an *IRAS* 100-μm sky flux that matched the value estimated subjectively to underly the nebular position. Diffuse interstellar clouds are not highly ionized enough to produce doubly ionized N^{2+} and O^{2+}, so that contamination from background emission to the nebular [N III] 57-μm and [O III] 52- and 88-μm lines is negligible unless the nebula falls close to a Galactic H II region. No offset spectra were therefore taken for nebulae observed with LWS AOT 2. The 122-μm line from singly ionized N^+ has been observed in some of our off-source spectra, probably produced by ionized diffuse clouds along the line of sight, thus contamination from Galactic background emission can be important for this line in some cases.

All the data presented here were processed with the LWS OLP Version 7 and were flux-calibrated using the LWS grating scan observations of Uranus (Swinyard et al. 1996). At the spectral resolving power of the LWS grating observations ($R \sim 150$–300), the far-IR spectrum of Uranus is generally featureless. However, detailed analysis of high signal-to-noise ratio (S/N) spectra of several astronomical sources (NGC 7027, AFGL 2688, IRC +10°216 and η Carina) calibrated with the Uranus grating observations, shows clear evidence of the presence of weak absorption features produced by the HD R(0) 112-μm fundamental pure rotational transition, and possibly also the R(1) 56-μm line, in the Uranus spectrum (Lim et al. 1997). These absorption features in the Uranus spectrum introduce artificial emission lines in the flux-calibrated target spectra, with an estimated (emission line) equivalent width of 0.014 ± 0.001 and 0.024 ± 0.004 μm, respectively. The presence of the HD R(0) absorption line in the Uranus spectrum has been confirmed by LWS FP observations of Uranus (M. Griffin, private communication), which yield an equivalent width consistent with the value estimated from our analysis of the above sources. Apart from the HD features, another three artificial emission features, probably also caused by some unknown absorption features in the Uranus spectrum, have been found near the nebular [N III] 57.33-μm line, at wavelengths of 57.04, 57.58 and 57.96 μm, with estimated equivalent widths of 0.008 ± 0.001, 0.008 ± 0.001 and 0.009 ± 0.001 μm, respectively. These features were only partially resolved by the LWS grating mode, so the estimates of their central wavelengths and equivalent widths are less secure. Except for NGC 7027, the [N III] 57-μm fluxes presented here were however hardly affected by these very weak spurious features. In the case of NGC 7027, because of the high electron density and strong dust continuum emission, its [N III] 57-μm emission line is relatively weak and has a small equivalent width. After correction for the spurious emission, the [N III] 57-μm line flux is about 40 per cent lower than that deduced before correction (Liu 1997).

Prior to the launch of *ISO*, several far-IR fine-structure lines had been measured with the Kuiper Airborne Observatory (KAO) for a number of PN (Melnick et al. 1981; Ellis & Werner 1984; Dinerstein, Lester & Werner 1985; Dinerstein et al. 1995; Rubin et al. 1997). A comparison of the new *ISO* LWS measurements with those of KAO was given by Liu (1997). The agreement is reasonably good for NGC 7009 and NGC 7027, observed with KAO by Rubin et al. (1997). There are however, some substantial discrepancies, especially when compared with some of the fluxes published by Dinerstein et al. (1985), probably caused by the calibration uncertainties in those early observations.

The end products of the LWS official pipeline were analysed using MIDAS.[1] After excluding data points flagged as invalid, each valid ramp measurement was assigned a weight proportional to the ramp length used to fit the measurement. For a given grating

[1] MIDAS is developed and distributed by the European Southern Observatory.

position, measurements from the individual scans obtained at this position and from the two adjacent positions were compared, and data which differed from the mean by more than 2 sigma were rejected. The measurements from the two adjacent grating positions were included in calculating the mean and sigma because at the sampling rate of 1/4 of the spectral resolution, the line profiles were well sampled. This clipping process was iterated, and then the remaining data points at the given grating position *only* were averaged to generate the final mean flux and standard error at the wavelength corresponding to that gating position. Apart from the standard analysis which includes scans in both directions, forward and backward scans were also separately analysed and compared. In general, except for detector SW1 and to some extent detector LW 2, which respectively covered 43–52 and 106–132 μm, the slopes of the continua from the forward and backward scans agreed reasonably well, as do fluxes for the emission lines.

For spectra obtained with the full grating scan mode (AOT 1), the sub-spectra from two adjacent detectors have some significant overlap in their wavelength coverage. By comparing the continuum levels in the overlapping region, it is thus possible to scale the sub-spectra from the 10 detectors such that they join smoothly to form a continuous spectrum over the whole 43–197 μm wavelength range covered by the LWS. In the current analysis, however, no scaling factors were applied to the individual sub-spectra. This was because the main interest of the current analysis was the emission line fluxes, not the dust continuum emission. Furthermore, many nebulae in our sample are well-evolved PN, with a characteristic spectrum of strong emission lines superimposed on a relatively weak dust continuum. For such sources, discrepancies in continuum levels between sub-spectra in their overlapping wavelength regions are likely to be dominated by uncertainties in the dark current subtraction, which do not affect the emission line fluxes, rather than being caused by sensitivity drifts of the detectors, which affect both the line and continuum fluxes. As we will show later, the emission line fluxes measured by adjacent detectors agree remarkably well over a wide dynamical range, without applying any scaling factors to the individual sub-spectra.

The emission line fluxes were measured using automatic Gaussian profile fitting. The local continuum level was determined by fitting a first order polynomial to data points outside the emission line, after clipping the bad points, and then subtracted. A line is defined as being detected if, after the continuum subtraction, the peak intensity at the expected wavelength of the line is two and half times or more higher than the standard deviation of the local continuum and if the line has a FWHM between half and three times the spectral resolution element. The line was then fitted with a Gaussian and its flux derived. Otherwise, an upper limit to the line flux was calculated, defined as the flux of a feature with a peak flux three times the continuum standard deviation and a width the same as the instrumental resolution element. Sample profiles of the fine-structure lines detected from NGC 3132, along with their Gaussian fits, are shown in Fig. 1.

The emission line fluxes derived from the individual detectors, and from individual observations when the object was observed more than once, are presented in Appendix A. For sources with a background measurement, lines fluxes derived from the on-source and off-source spectra as well as those derived after subtracting the off-source spectrum from the on-source one, are listed separately. Fluxes deduced from the 'On – Off' spectrum are preferred over values obtained by subtracting the off-source fluxes from the one-source ones, since for nebulae embedded in strong background emission, the spectra have significant fringing at wavelengths $\gtrsim$120 μm, which affects determinations of the local continuum level and thus the accuracy of the line fluxes derived, especially for weak lines such as [O I] 146 μm. On the other hand, the fringing is largely removed after subtracting the off-source spectrum from the on-source one (Liu 1997).

For the AOT 1 observations, apart from the [N II] 122-μm line, all the fine-structure lines were measured simultaneously by two

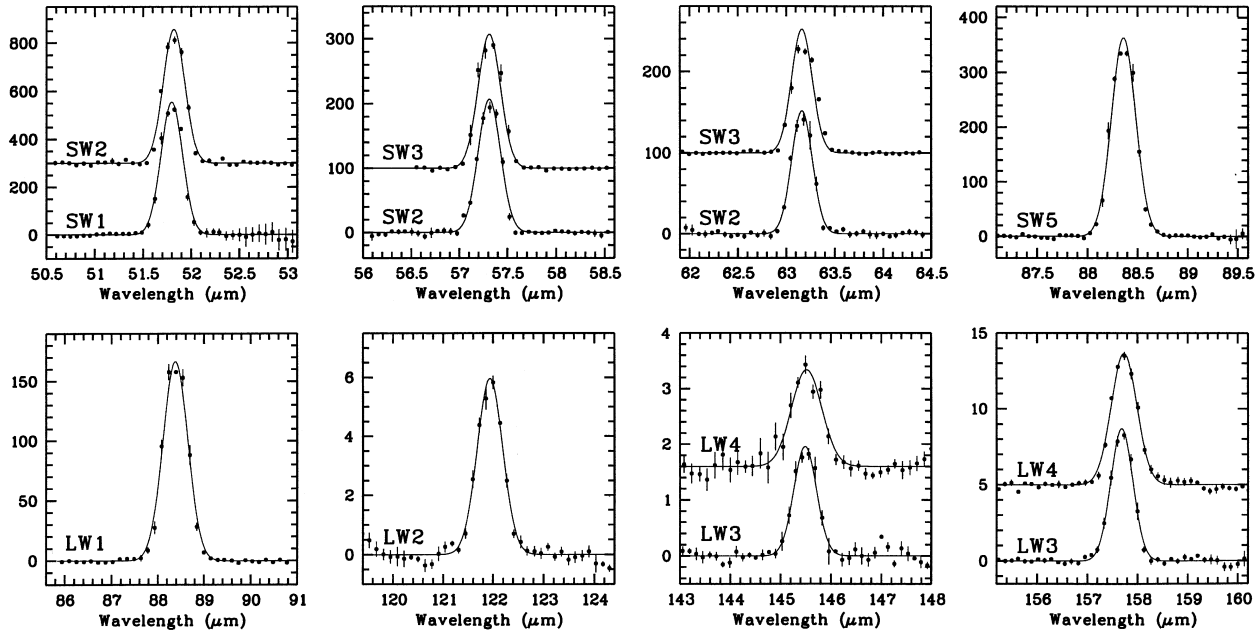

Figure 1. Sample profiles of the fine-structure lines detected from NGC 3132. The underlying continuum has been subtracted locally. The solid curves are Gaussian line profile fits to the observed data points. The flux is in units of 10^{-12} erg cm^{-2} s^{-1} μm^{-1}.

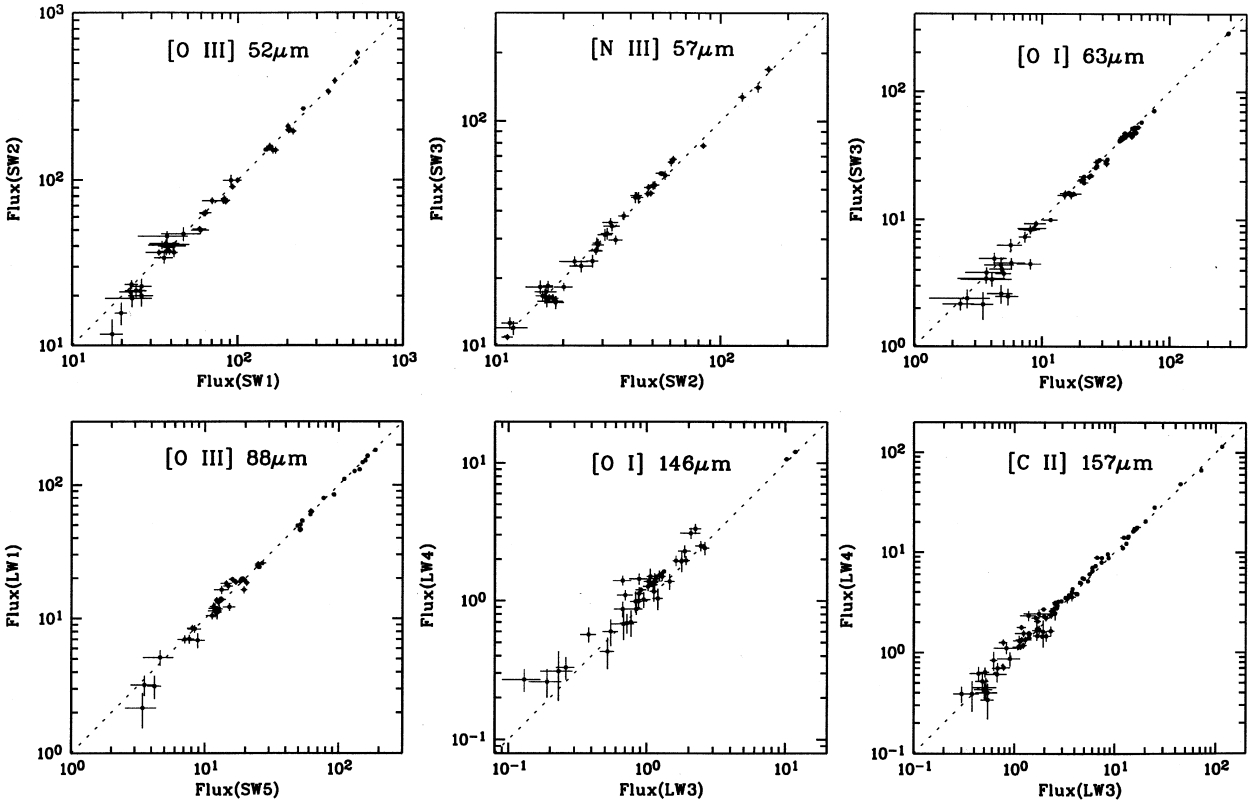

Figure 2. Comparison of the LWS emission line fluxes measured by adjacent detectors. The flux is in units of 10^{-12} erg cm^{-2} s^{-1} μm^{-1}.

adjacent detectors. In Fig. 2, we compare the fluxes derived from the two detectors for each line. In all cases, over the entire dynamical range of the lines observed, the fluxes yielded by the two independent detectors agree remarkably well. There is some evidence that for the [N III] 57-μm line, over a limited flux range, the fluxes given by detector SW3 are systematically higher than those yielded by SW2, but only at a level of ≲10 per cent. Somewhat larger discrepancies, up to about 25 per cent, are seen between the weak [O I] 146-μm line fluxes measured by the LW3 and LW4 detectors.

The lines fluxes deduced from adjacent detectors were averaged, with weights proportional to the inverse square of the uncertainties given by the Gaussian line profile fitting. The adopted line fluxes are presented in Table 2. For sources with background measurements, the fluxes are those deduced after subtracting the off-source spectrum from the on-source one. For sources without a background measurement, it is possible that the tabulated fluxes of the neutral region lines, [O I] 63 and 146 μm and [C II] 158 μm, and possibly also the low-excitation [N II] 122-μm line, may contain some contributions from Galactic background emission. For lines from the ionized regions, [O III] 52 and 88 μm, and [N III] 57 μm, contamination from Galactic background emission should be negligible.

Two objects in our sample, Lo 14 and Mz 3, require some comment, see Appendix B.

3 ELECTRON DENSITIES FROM THE [O III] 52 μm/88 μm RATIO

The [O III]52 μm/88 μm ratios and the electron densities deduced from them are presented in Table 3. The densities were deduced using a six-level atomic model of O^{++}, employing the collision strengths of Aggarwal (1983) and the Einstein spontaneous transition probabilities of Nussbaumer & Storey (1981a). The 52 μm/88 μm flux ratio as a function of N_e for $T_e = 5000$, 10 000 and 15 000 K is plotted in Fig. 3. Replacing the collision strengths for the fine-structure levels of the ^3P ground term of O^{++} with those of Lennon & Burke (1994) yields almost identical results. For a typical 52 μm/88 μm ratio of 5, values of N_e derived for $T_e = 5000$ and 15 000 K differ from that for $T_e = 10\,000$ K by less than 0.1 dex. The results become more sensitive to the adopted T_e for densities higher than 3×10^4 cm^{-3}. However, at such high densities, the 52 μm/88 μm ratio is no longer a useful density diagnostic. Here we have adopted a constant T_e of 10 000 K for all PN in our sample. If required, N_es for other values of T_e can be easily derived from the line ratios given in the table. No errors are provided for the derived values of N_e, since the line flux errors listed in Table 2 and in Table A1, deduced from Gaussian line profile fitting, did not include systematic errors, caused by for example uncertainties in the flux calibration, and are therefore likely to have been underestimated in many cases, given the high signal-to-noise ratio (S/N) of the LWS spectra. The systematic errors are difficult to estimate but are likely to be less than 20 per cent.

Electron densities deduced from the [O III] 52 μm/88 μm ratio for 21 PN in the current sample, based on line fluxes measured from the LWS spectra processed with OLP Version 6.0, were previously presented by Liu (1997). The results are in good agreement with the new values presented in Table 3, with discrepancies of ≲0.1 dex except for IC 5117 and NGC 6781 and 6886, where the discrepancies amount to a factor of two. For IC

5117 and NGC 6886, the discrepancies are mainly caused by the large flux uncertainties of the weak [O III] 88-μm line (c.f Table 2). For NGC 6781, the 52-μm line flux based on the new Version 7 OLP product is 14 per cent higher than that measured on the same spectrum processed with the Version 6 OLP. In contrast, the new 88-μm line flux is 18 per cent *lower*, leading to a significant difference in the 52 μm/88 μm ratio. The cause of the discrepancy is unclear. Note also the large discrepancy between the 88-μm line

Table 2. Adopted LWS line fluxes in units of 10^{-12} erg cm^{-2} s^{-1}.

Source	[N II] 122 μm	[N III] 57 μm	[O III] 52 μm	[O III] 88 μm	[O I] 63 μm	[O I] 146 μm	[C II] 158 μm
BD+30°3639	0.73 ± 0.12				73 ± 2	1.69 ± 0.07	4.78 ± 0.08
CPD−56°8032					28 ± 1	0.86 ± 0.06	1.71 ± 0.06
Cn 1-5		12.0 ± 0.8	24 ± 2	8.4 ± 0.5	2.6 ± 0.4		
Hb 12					6.1 ± 0.6		1.2 ± 0.1
He 2-113					43 ± 1	1.13 ± 0.06	1.94 ± 0.07
He 2-131	0.5 ± 0.2				15.8 ± 0.9	0.50 ± 0.05	0.96 ± 0.06
HD 44179					2.8 ± 0.4		
Hu 2-1			9 ± 2	1.5 ± 0.5			
IC 418	0.84 ± 0.06	16.6 ± 0.7	77 ± 3	12.9 ± 0.5	53 ± 2	1.17 ± 0.07	5.2 ± 0.1
IC 3568	0.12 ± 0.04	6.0 ± 0.4	38 ± 1	19.4 ± 0.5			
IC 4191		5 ± 2	48 ± 4	13.3 ± 0.9			
IC 4634			36 ± 2	11.1 ± 0.6			
IC 4406	1.3 ± 0.1	25 ± 1	92 ± 3	51 ± 1	29.2 ± 0.9	0.93 ± 0.05	3.41 ± 0.06
IC 4997					4.6 ± 0.4		
IC 5117			7 ± 1	1.1 ± 0.3	16.2 ± 0.6	0.44 ± 0.04	1.40 ± 0.04
IRAS 21282+5050					29 ± 1	1.31 ± 0.08	3.4 ± 0.2
Lo 14 on-source[a]	43 ± 1	50 ± 1	36 ± 2	61 ± 1	30.6 ± 0.6	4.4 ± 0.3	115 ± 1
Lo 14 off-source[b]	9.7 ± 0.3	3.6 ± 0.4		11.9 ± 0.8	10.0 ± 0.3	1.6 ± 0.3	46.1 ± 0.5
M 1-42		28 ± 1	40 ± 2	18.0 ± 0.7	2.9 ± 0.4		
M 1-92					3.0 ± 0.5		
M 2-36		6.3 ± 0.6	22 ± 2	7.6 ± 0.7			
M 2-55		9.1 ± 0.6	22 ± 1	26.0 ± 0.7	4.8 ± 0.5		1.7 ± 0.1
M 2-9					51 ± 1	1.93 ± 0.09	4.0 ± 0.1
Mz 3[c]	11.1 ± 0.5	35 ± 1	18 ± 1	7.0 ± 0.4	21.7 ± 0.6	0.75 ± 0.07	16.0 ± 0.2
Mz 3 off-source[d]	4.5 ± 0.4			2.6 ± 0.5	5.6 ± 0.3		20.3 ± 0.2
NGC 40	3.2 ± 0.1	17 ± 1	20 ± 3	11.9 ± 0.8	22.1 ± 0.9	0.75 ± 0.07	8.1 ± 0.1
NGC 2346	0.97 ± 0.07	11.0 ± 0.3	23 ± 1	24.8 ± 0.7	8.2 ± 0.4	0.28 ± 0.03	2.82 ± 0.07
NGC 3132	3.8 ± 0.2	62 ± 2	156 ± 4	110 ± 2	40.9 ± 0.9	1.18 ± 0.06	5.1 ± 0.1
NGC 3242		31 ± 1	347 ± 9	155 ± 3			
NGC 3918		31 ± 1	203 ± 7	63 ± 2	15.4 ± 0.9	0.54 ± 0.07	0.48 ± 0.09
NGC 5189	1.3 ± 0.1	65 ± 2	96 ± 6	87 ± 1	6.5 ± 0.9	0.22 ± 0.04	0.48 ± 0.07
NGC 5315	0.60 ± 0.15	18 ± 1	50 ± 2	11.7 ± 0.9	46 ± 1	1.00 ± 0.07	1.53 ± 0.08
NGC 5882		29 ± 2	171 ± 6	59 ± 2			
NGC 6072	1.9 ± 0.2	26.8 ± 0.9	64 ± 2	54 ± 1	20.2 ± 0.6	0.85 ± 0.06	3.9 ± 0.1
NGC 6153		144 ± 4	540 ± 12	164 ± 4	2.2 ± 0.6		
NGC 6302	7.5 ± 0.6	167 ± 4	157 ± 5	49 ± 1	284 ± 7	10.5 ± 0.2	13.7 ± 0.4
NGC 6537	3.1 ± 0.3	48 ± 1	41 ± 2	16.6 ± 0.7	44 ± 1	2.0 ± 0.2	2.3 ± 0.2
NGC 6543		126 ± 4	511 ± 13	149 ± 4	4.6 ± 0.4	0.23 ± 0.04	0.44 ± 0.07
NGC 6567			35 ± 3	8.3 ± 0.6			
NGC 6572		24 ± 1	155 ± 6	25.2 ± 0.9	49 ± 2	1.16 ± 0.09	2.1 ± 0.1
NGC 6578		31 ± 3	135 ± 6	44 ± 2			
NGC 6720	3.9 ± 0.2	80 ± 2	262 ± 5	184 ± 2	58.1 ± 0.8	1.82 ± 0.07	6.8 ± 0.2
NGC 6741		7 ± 3	26 ± 2	5.4 ± 0.4			
NGC 6781	3.0 ± 0.2	58 ± 1	151 ± 3	104 ± 1	25.5 ± 0.5	0.98 ± 0.08	6.1 ± 0.2
NGC 6790			12 ± 2				
NGC 6826		38 ± 1	204 ± 5	78 ± 2			0.32 ± 0.07
NGC 6884		9 ± 2	57 ± 3	17.2 ± 0.9			
NGC 6886			15 ± 2	3.0 ± 0.4			
NGC 7009		57 ± 2	389 ± 11	129 ± 3			
NGC 7027	0.49 ± 0.05	17.6 ± 0.6	122 ± 6	14.0 ± 0.6	606 ± 17	21.3 ± 0.3	42.6 ± 0.5
NGC 7662		18.6 ± 0.7	205 ± 6	78 ± 2			0.18 ± 0.08
Vy 2-2					8.3 ± 0.6		1.0 ± 0.2

[a] Emission probably associates with the nearby strong radio source G 331.5 − 0.1; cf. Appendix B for details.
[b] Emission probably dominated by a background H II region; cf. Appendix B for details.
[c] Without corrections for the Galactic background emission; possible contamination from a nearby H II region; c.f Appendix B.
[d] Emission dominated by a background H II region; c.f Appendix B.

Table 3. [O III] 52 μm/88 μm flux ratios and the electron densities N_e deduced from it. The results are compared to N_es derived from the optical [Ar IV] λ4740/λ4711 and [Cl III] λ5537/λ5517 doublet ratios.

Source	[O III] 52 μm/88 μm	[O III] log N_e (cm^{-3})	[Ar IV] log N_e (cm^{-3})	[Cl III] log N_e (cm^{-3})
Cn 1-5	2.86	3.06	3.35	3.46
Hu 2-1	6.00	3.67		3.39
IC 418	5.97	3.66		4.05
IC 3568	1.96	2.80	3.40	
IC 4191	3.61	3.23	4.09	4.05
IC 4634	3.24	3.15	3.87	3.72
IC 4406	1.80	2.73	3.09	2.99
IC 5117	6.36	3.73	4.76	4.72
Lo 14[a]	.596	≈0		
M 1-42	2.22	2.88	2.78	3.23
M 2-36	2.89	3.07	3.64	3.68
M 2-55	.846	2.06		
Mz 3	2.57	2.99		4.17
NGC 40	1.68	2.69		3.30
NGC 2346	.927	2.15	2.57	
NGC 3132	1.40	2.55	2.69	2.83
NGC 3242	2.24	2.89	3.43	3.20
NGC 3918	3.22	3.14	3.66	3.70
NGC 5189	1.10	2.33		
NGC 5315	4.27	3.36	4.08	4.37
NGC 5882	2.90	3.07	3.58	3.44
NGC 6072	1.18	2.39	3.26	
NGC 6153	3.29	3.16	3.34	3.60
NGC 6302	3.20	3.14	4.23	4.41
NGC 6537	2.47	2.86		4.52
NGC 6543	3.43	3.19	3.59	3.68
NGC 6567	4.22	3.35	3.94	3.82
NGC 6572	6.15	3.70	4.34	4.26
NGC 6578	3.07	3.11	3.57	3.25
NGC 6720	1.42	2.55	2.76	2.95
NGC 6741	4.81	3.46	3.82	3.65
NGC 6781	1.45	2.57		2.93
NGC 6826	2.62	3.00	3.30	3.15
NGC 6884	3.31	3.17	3.91	3.82
NGC 6886	5.00	3.49	3.87	4.30
NGC 7009	3.02	3.10	3.60	3.57
NGC 7027	8.71	4.26	4.74	4.67
NGC 7662	2.63	3.00	3.50	3.39

[a] From Lo 14 on-source measurement without background subtraction; cf. footnotes to Table 2 and Appendix B. The observed 52 μm/88 μm ratio for Lo 14 is lower than, but consistent within the uncertainties with the low density limit of 0.623.

fluxes of NGC 6781 yielded by detectors SW5 and LW1 (Table A1). The discrepancy is almost twice as large as found on the same spectrum when processed with the Version 6 OLP.

Liu (1997) showed that the electron densities derived from the [O III] 52 μm/88 μm ratio are systematically lower than those deduced from the optical [Ar IV] λ4740/λ4711 and [Cl III] λ5537/λ5517 doublet ratios for the same object, and interpreted the result as due to density inhomogeneities in the nebula. In Table 3, the electron densities derived from the optical [Ar IV] and [Cl III] lines are presented in the last two columns. Except for a few cases, they were derived using high S/N ratio, high spectral resolution CCD

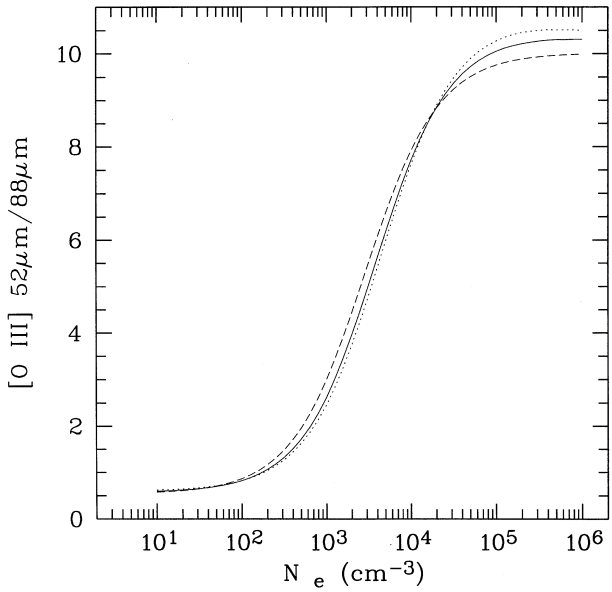

Figure 3. The [O III] 52 μm/88 μm flux ratio as a function of electron density N_e for (a) $T_e = 10\,000$ K (solid line); (b) $T_e = 5000$ K (dashed line) and (c) $T_e = 15\,000$ K (dotted line).

spectra obtained during a deep optical spectroscopic survey of a large sample of Galactic PN (cf. Liu et al. 2000). Amongst the nebulae listed in Table 3, the optical spectra of IC 3568, NGC 40, 6543, 6572, 6720, 6741, 6781, 6826, 6884, 7009, 7027 and 7662 were obtained by uniformly scanning the 4-arcmin-long slit of the ISIS double spectrograph mounted on the WHT 4.2-m telescope across the entire nebular surface, yielding an average spectrum for the whole nebula. IC 4191, IC 4406, NGC 3132, 3242, 3918, 5315, 5882, 6072 and 6153 were uniformly scanned with the Boller & Chivens long-slit spectrograph mounted on the ESO 1.52-m telescope. For these scanned nebulae, the electron densities derived from the [Ar IV] and [Cl III] doublet ratios are directly comparable to those derived from the [O III] 52 μm/88 μm ratio, as both the optical and the IR observations sample the whole nebula. Optical spectra of Cn 1-5, IC 4634, M 1-42, M 2-36, Mz 3, NGC 6302, 6537 ([Cl III] lines only), 6567 and 6578 were obtained with the ESO 1.52-m telescope using a fixed long slit, usually positioned at the nebular centre and through the brightest parts of the nebula. Amongst them, Cn 1-5, IC 4634, M 1-42 and M 2-36 have an angular diameter of only a few arcsecs, thus the electron densities deduced from the long-slit spectra should be representative of the whole nebula. The S/N ratio of the scanned spectrum of NGC 6781 was not good enough to measure the [Ar IV] and [Cl III] doublets accurately. Its [Cl III] density was derived from a fixed long-slit spectrum obtained at the ESO 1.52-m telescope. Similarly, the [Ar IV] density of IC 4406 was derived from a fixed long-slit spectrum obtained at the ESO 1.52-m telescope. For a few nebulae for which we have no optical data, the [Ar IV] and [Cl III] densities were derived using fluxes published in the literature. The references are: IC 5117, Aller & Czyzak (1979); Hu 2-1, Aller & Czyzak (1983); NGC 2346, Peimbert & Torres-Peimbert (1987); IC 418, Hyung, Aller & Feibelman (1994a); NGC 6886, Hyung, Keyes & Aller (1995).

The [Ar IV] and [Cl III] densities were derived using a five-level atomic model. The collision strengths of Zeippen, Butler & Le Bourlot (1987) for Ar^{3+} and of Butler & Zeippen (1989) for Cl^{2+} were used. For both ions, the transition probabilities were taken

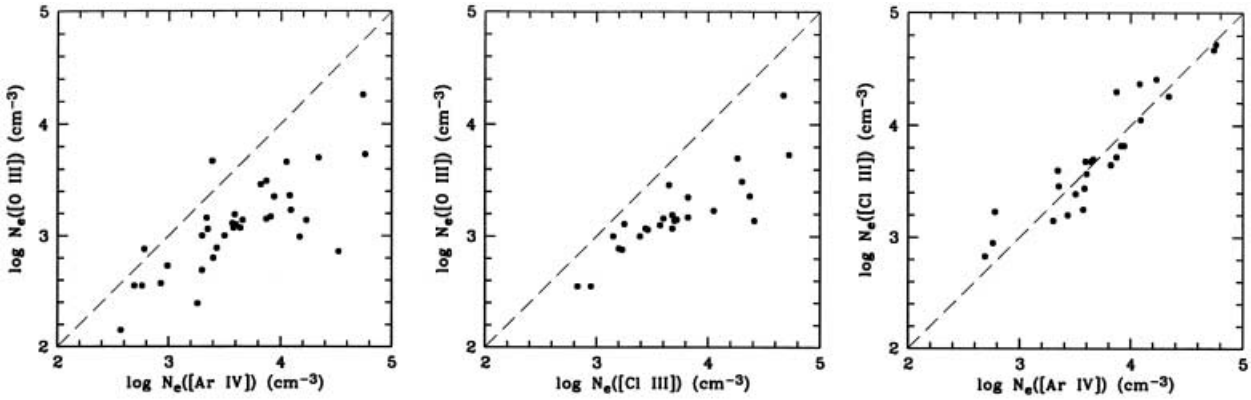

Figure 4. Comparison of the electron densities derived from the intensity ratios of [O III] 52 μm/88 μm, [Ar III] λ4740/λ4711 and [Cl III] λ5537/λ5517.

from Mendoza & Zeippen (1982). Upgrading the Ar^{3+} collision strengths to those calculated more recently by Ramsbottom, Bell & Keenan (1997) yields densities slightly lower than those derived here, by less than 0.1 dex except for densities lower than $10^3\,cm^{-3}$ (Keenan et al. 1997). At such low densities, the [Ar IV] doublet ratio is however no longer a sensitive density-diagnostic.

The electron densities deduced from the [O III] 52 μm/88 μm ratio, and from the [Ar IV] λ4740/λ4711 and [Cl III] λ5537/λ5517 doublet ratios are compared in Fig. 4. Consistent with the earlier finding of Liu (1997), there is good agreement between the densities derived from the [Ar IV] doublet ratio and from the [Cl III] ratio, but both the [Ar IV] and [Cl III] doublet ratios yield densities that are systematically higher than those derived from the [O III] 52 μm/88 μm ratio. There is a clear trend in that the discrepancy becomes larger at higher densities.

Cl^+ and Ar^{2+} have ionization potentials of 23.8 and 40.7 eV respectively, comparable to the value of 35.1 eV for O^+. Thus the [Ar IV] and [Cl III] lines should arise from similar ionized regions as the [O III] lines. The systematically smaller values of the [O III] densities compared to the [Ar IV] and [Cl III] densities are therefore unlikely to be caused by ionization stratification nor by uncertainties in the atomic data, given the good agreement between the [Ar IV] and [Cl III] densities. The [Ar IV] λλ4711, 4740 and [Cl III] λλ5517, 5537 lines have however critical densities N_c of 1.4×10^4, 1.3×10^5, 6.4×10^3 and $3.4\times10^4\,cm^{-3}$ respectively, much higher than the critical densities of $N_c = 3500$ and $1500\,cm^{-3}$ for the [O III] 52- and 88-μm lines. Thus the low values of the [O III] densities can be explained if the nebulae are not homogeneous but contain condensations with electron densities significantly higher than the critical densities of the [O III] far-IR lines. For an inhomogeneous nebula, the [O III] far-IR lines will be suppressed in regions of high density by collisional de-excitation, thus their emission will be biased towards regions of lower density. In contrast, the [Ar IV] and [Cl III] lines will be much less affected by collisional de-excitation owing to their higher critical densities. As a result, for an inhomogeneous nebula the [O III] far-IR lines will yield an average density lower than these values given by the [Ar IV] and [Cl III] lines. Dinerstein et al. (1985) measured the [O III] 52- and 88-μm lines using the KAO for six PN and found that the densities deduced from the 52 μm/88 μm ratio were consistent within the errors with those derived from the [O II] λ3729/λ3726 ratio. However, the [O II] lines, as well as the [S II] λλ6716, 6731 lines (whose ratios serve as the most frequently used density-diagnostics in the optical), have critical densities that are comparable to or only slightly higher than those of the [O III] far-IR fine-structure lines. Moreover, in most nebulae O^+ and S^+ are only trace ionic species, and are present only in a thin transition layer near ionization fronts. Thus both the [O II] and the [S II] optical doublet ratios are not suitable for searching for ionized high density nebular condensations.

The presence of nebular density inhomogeneities will affect not only the N_e yielded by the 52 μm/88 μm ratio, it will also lead to an overestimated T_e calculated from the [O III] (λ4959+λ5007)/(λ52 μm+λ88 μm) ratio. The electron temperature derived from the [O III] (λ4959+λ5007)/λ4363 nebular to auroral line ratio, the standard temperature diagnostic in optical nebular analyses, can also be overestimated, but only if the electron densities in the condensations are sufficiently high, say $\sim10^6\,cm^{-3}$, higher than the critical densities of the λλ4959, 5007 nebular lines ($N_c = 6.9\times10^5\,cm^{-3}$) but lower than that of the λ4363 auroral line ($N_c = 2.5\times10^7\,cm^{-3}$). Viegas & Clegg (1994) suggest that collisional de-excitation of the [O III] nebular lines in such high-density regions may be responsible for the systematically lower electron temperatures deduced from the nebular continuum Balmer discontinuity compared to those yielded by the [O III] nebular to auroral line ratio, as observed in many Galactic PN (Liu & Danziger 1993). Detailed discussion of density inhomogeneities and temperature fluctuations in the unusual PN NGC 6153 and their effects on plasma-diagnostics and ionic abundance determinations is given by Liu et al. (2000). They show that while their observations suggest density inhomogeneities, the presence of a substantial amount of gas in condensations with densities in excess of $10^6\,cm^{-3}$ can be ruled out by the observed relative intensities of high order hydrogen Balmer lines, unless at the same time those high-density condensations are also H-deficient, such as those found in the 'born-again' PN A 30 and A 78 (Jacoby 1979; Hazard et al. 1980; Jacoby & Ford 1983).

4 IONIC ABUNDANCES OF N AND O

The ionic abundances N^+/H^+, N^{2+}/H^+ and O^{2+}/H^+ derived respectively from the [N II] 122-μm, [N III] 57-μm, and [O III] 52- and 88-μm lines are given in Table 4. No corrections for interstellar extinction are needed for these far-IR fine-structure lines. Ionic abundances ratios relative to H^+ were derived using the extinction-corrected Hβ fluxes listed in the second column of Table 4, calculated from $\log I(H\beta) = \log F(H\beta) + c_r(H\beta)$, where $F(H\beta)$ and $c_r(H\beta)$ are respectively the observed Hβ flux and the logarithmic extinction at Hβ. Values of $F(H\beta)$ and $c_r(H\beta)$ were

Table 4. Ionic abundances from far-IR fine-structure lines.

Source	$\log I(\mathrm{H}\beta)$ (cgs)	$\frac{N^+}{H^+}$ (10^{-5})	$\frac{N^{2+}}{H^+}$ (10^{-5})	$\frac{O^{2+}}{H^+}$ (10^{-5})	$\frac{N^{2+}}{O^{2+}}$
Cn 1-5	−10.85		16.1	29.2	0.55
Hu 2-1	−10.46			9.85	
IC 418	−9.23	1.22	1.63	4.88	0.33
IC 3568	−10.62	0.69	3.26	23.0	0.14
IC 4191	−10.29		2.45	19.0	0.13
IC 4634	−10.39			16.5	
IC 4406	−10.48	4.75	9.05	39.0	0.23
IC 5117	−10.17			4.35	
M 1-42	−10.93		34.5	51.4	0.67
M 2-36	−11.18		18.3	57.8	0.32
M 2-55	−10.92		5.44	24.1	0.22
Mz 3[a]	−9.68	10.7	2.84	1.40	2.03
NGC 40	−9.81	2.33	1.26	1.80	0.70
NGC 2346	−10.66	2.22	3.77	13.7	0.28
NGC 3132	−10.15	4.73	8.68	29.4	0.30
NGC 3242	−9.62		1.90	22.0	0.09
NGC 3918	−9.64		2.92	16.4	0.18
NGC 5189	−9.89	0.64	4.20	9.68	0.43
NGC 5315	−9.87	1.95	4.26	8.81	0.48
NGC 5882	−9.96		5.08	27.0	0.19
NGC 6072	−10.31	2.66	4.75	17.0	0.28
NGC 6153	−9.67		15.0	47.6	0.32
NGC 6302	−9.16	2.97	5.20	4.20	1.24
NGC 6537	−9.92	4.00	5.63	4.89	1.15
NGC 6543	−9.49		9.14	30.7	0.30
NGC 6567	−10.31			16.8	
NGC 6572	−9.34		3.30	13.6	0.24
NGC 6578	−10.28		12.1	46.2	0.26
NGC 6720	−9.97	3.21	7.40	32.5	0.23
NGC 6741	−10.30		5.40	14.2	0.38
NGC 6781	−9.99	2.67	5.73	19.8	0.29
NGC 6790[b]	−10.11			9.56	
NGC 6826	−9.91		5.32	27.2	0.20
NGC 6884	−10.24		3.55	18.9	0.19
NGC 6886	−10.60			17.0	
NGC 7009	−9.63		4.91	29.6	0.16
NGC 7027	−8.74	0.91	2.06	7.99	0.26
NGC 7662	−9.79		1.98	20.7	0.10

[a] Without background emission correction; possible contamination from adjacent H II regions; cf. Appendix B.
[b] Assuming $\log N_e = 10^4\,\mathrm{cm}^{-3}$, approximately the average density yielded by the [S II], [Cl III] and [Ar IV] optical doublet ratios (French 1981; Aller & Czyzak 1979).

taken from the compilation of Cahn, Kaler & Stanghellini (1992), except for $F(\mathrm{H}\beta)$ of M 2-36, where we have adopted the value measured by Liu et al. (in preparation) using the ESO 1.52-m telescope with an eight-arcsec wide slit. Our procedure for abundance calculations was equivalent to normalizing the observed ionic fine-structure line fluxes to the 5-GHz radio free–free flux, since $c_r(\mathrm{H}\beta)$ was derived by comparing the observed $F(\mathrm{H}\beta)$ and the radio fluxes at 5 GHz (or at a higher frequency such as 14.7 GHz for nebulae which might be optically thick at 5 GHz; cf. Cahn et al. 1992). The ionic abundances were deduced using the electron density derived from the [O III] 52 μm/88 μm ratio (Table 3). A constant temperature of 10 000 K was assumed for all nebulae. The small dependence of the results on electron temperature, less than 20 per cent over the range from 8000–15 000 K, has been neglected. The emissivity of the [N III] 57-μm line was calculated using a five-level atomic model with the transition probabilities and collision strengths taken from Fang, Kwong & Parkinson (1993) and Blum & Pradhan (1992), respectively. For [N II], a six-level atomic model was used, using the collision strengths of Stafford et al. (1994) and the transition probabilities of Nussbaumer & Rusca (1979). The emissivity of Hβ was calculated from the Case B effective recombination coefficients of Storey & Hummer (1995).

The ionic abundance relative to H^+ deduced from a collisionally excited line becomes directly proportional to the adopted electron density when the nebular electron density is significantly higher than the critical density of the collisional line, $N_e \gg N_c$. Both the [O III] and [N III] far-IR fine-structure lines have relatively low critical densities, $N_c \sim (0.5\text{–}4) \times 10^3\,\mathrm{cm}^{-3}$, comparable to or lower than the typical electron density of many PN in our sample. The critical density of the [N II] 122-μm line is even lower, $N_c = 270\,\mathrm{cm}^{-3}$. The strong dependence of the O^{2+}/H^+ ratio derived from the 52- and 88-μm lines is partly alleviated by adopting the electron density yielded by the 52 μm/88 μmratio. Since the [N III] 57-μm line has a critical density comparable to the [O III] 52- and 88-μm lines, the electron density yielded by the 52 μm/88 μm ratio should also be representative of the average density of the 57-μm line emitting zones.

A weak [N II] 122-μm line was marginally detected from the young dense PN He 2-131. The corresponding N^+/H^+ abundance ratio cannot be derived because the appropriate electron density, which could be high, is unknown. As discussed in Appendix B, contamination of the [N III] and [O III] lines detected in the on-source spectrum of Mz 3 from a nearby H II region is probably unimportant. No attempt was made to subtract the background emission using the off-source spectrum, given the complicated structure of the H II region.

The PN N^{2+}/O^{2+} abundance ratios derived from the LWS observations are listed in the last column of Table 4. Note that although the N^{2+}/H^+ and O^{2+}/H^+ abundance ratios derived from the [N III] 57-μm line and from the [O III] 52- and 88-μm lines are sensitive to the adopted electron density, N^{2+}/O^{2+} deduced from the 57 μm/(52 μm + 88 μm) ratio depends only weakly on N_e. This is demonstrated in Fig. 5 where we compare the 52 μm/57 μm, 88 μm/57 μm and (52 μm + 88 μm)/57 μm emissivity ratios as a function of N_e. Fig. 5 shows that the (52 μm + 88 μm)/57 μm emissivity ratio, and consequently the N^{2+}/O^{2+} value derived from the corresponding line flux ratio, has a very small density dependence, varying by less than a factor of two over the entire density range. We show in Appendix B that the ionic emission lines detected in the LWS spectrum centred on Lo 14 are possibly associated with the Galactic radio source G 331.5 − 0.1, whereas lines detected in its off-source spectrum are likely dominated by H II regions in the Galactic plane. The radio free–free fluxes falling within the LWS beam for these two spectra are not known, so the N^{2+} and O^{2+} ionic abundances relative to H^+ cannot be deduced. From the 57 μm/(52 μm + 88 μm) ratio derived from the spectrum centred on Lo 14 (without correcting for background emission) we find $N^{2+}/O^{2+} = 0.60$. Similarly, from the 57 μm/52 μm ratio measured in the off-source spectrum, we find $N^{2+}/O^{2+} = 0.12$, which is identical to the solar N/O ratio.

N^0, N^+, N^{2+} and N^{3+} have ionization potentials of 14.5, 29.6, 47.4 and 77.5 eV, respectively, comparable to the values of 13.6, 35.1, 54.9 and 77.4 eV for the corresponding ionization stages of O. Thus to a very good approximation, $N/O = N^{2+}/O^{2+}$. The N/O ratios derived from the LWS observations cover a wide range

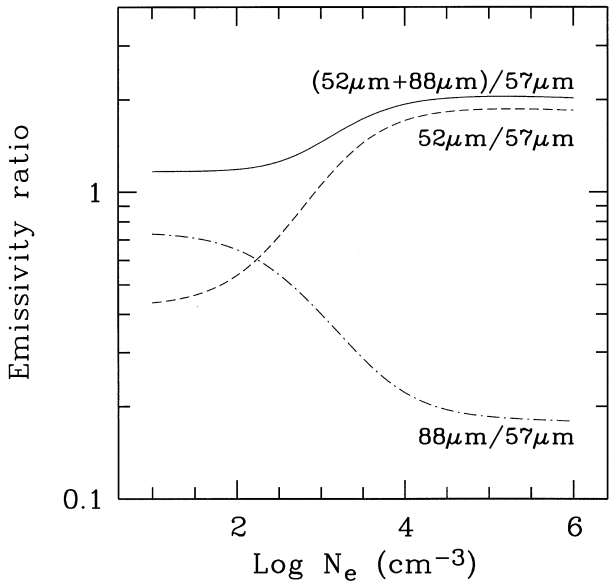

Figure 5. Emissivity ratios of the [O III] 52- and 88-μm lines relative to the [N III] 57-μm line as a function of electron density N_e. An electron temperature of $T_e = 10^4$ K was assumed.

of values, ranging from ∼0.1, i.e. nearly identical to the solar value of 0.12 (Anders & Grevesse 1989; Grevesse & Noels 1993), to the extreme value of 2.03 for Mz 3. The extremely high N/O ratio of Mz 3 derived from the LWS observation of the far-IR fine-structure lines is supported by our unpublished optical observations, from which we find $N^+/O^+ = 2.14$. PN with $He/H \gtrsim 0.125$ and $N/O \gtrsim 0.3$ were classified as Type-I by Peimbert & Torres-Peimbert (1983). Type-I PN are often bipolar, showing pronounced filamentary structure and are believed to have evolved from more massive progenitor stars than Type-II PN. In a more recent abundance study of a large sample of Galactic PN, Kingsburgh & Barlow (1994) redefined Type-I PN as those objects that have experienced envelope-burning conversion to nitrogen of dredged-up primary carbon, i.e. PN with a N/O ratio greater than the (C+N)/O ratio of H II regions in the host galaxy, with the latter being 0.8 for our own Galaxy. According to the revised criterion of Kingsburgh & Barlow (1994), only three objects in our sample, NGC 6302 and 6537 and Mz 3, all bipolar, are Type-I PN.

5 PHYSICAL CONDITIONS IN THE PHOTODISSOCIATION REGIONS

Neutral region emission has been detected from over half of the nebulae in our sample. For 24 of them, all three major PDR cooling lines, i.e. [O I] 63 and 146 μm and [C II] 158 μm, have been detected.[2] In an excellent review paper, Watson (1983) first showed that the [O I] 63 μm/146 μm ratio, combined with the ratio of the 63-μm line to the [C II] 158-μm line, can be used to derive the temperatures and densities of PDRs. Since this method involves lines from two different atomic species of C and O, it requires knowledge of the C/O abundance ratio of the emitting gas. In Fig. 6, the observed 63 μm/146 μm ratios are plotted against the 63 μm/158 μm ratios, normalized to the cosmic (solar) C/O ratio of 0.5. Loci for a range of values of temperature and density are overplotted. The nebulae are labelled by their sequence number in Table 5. Three- and two-level atomic models were used to calculate the level populations of the fine-structure levels of the O^0 and C^+ ground terms respectively. Collisional excitation by atomic hydrogen was assumed. The transition probabilities for the [C II] and [O I] fine-structure lines were taken from Nussbaumer & Storey (1981b) and Baluja & Zeippen (1988) respectively, and the collision strengths for H impacts are from Launay & Roueff (1977a,b) for $T < 1000$ K and from Keenan et al. (1986) and Péquignot (1990, 1996) for higher temperatures.

The temperatures and densities derived from the 63 μm/146 μm and 63 μm/158 μm ratios are given in columns 7 and 8 of Table 5. The C/O abundance ratios adopted for individual nebulae are listed in column 3. Columns 4 and 5 gives the C/H abundances [in units where $\log N(H) = 12$] and the nebular distances. The references for the C/O and C/H ratios (Refs. 1–21, 32) and distances (Refs. 2, 22–31) are given in column 6 and listed in the footnotes. No reliable C/O abundance ratios are available for IC 4406, IRAS 21282+5050, M 2-9 and NGC 6072 and 6781, so a cosmic value of 0.5 was adopted. The C/H abundances for these nebulae are then obtained from the observed O/H abundances. For IRAS 21282+5050, a solar C/H ratio was assumed. This PPN is probably C-rich, so that its C/O and C/H ratios may be higher than the solar values adopted here, with the consequence that higher temperatures and densities for its PDR would then be deduced from Fig. 6. The *absolute* elemental abundances of C, N and O relative to H are extremely uncertain for Mz 3, and a cosmic C/O ratio of 0.5 together with the solar C/H abundance of 8.55 (Anders & Grevesse 1989) were adopted for the purpose of the current analysis. As discussed in Appendix B, the 158-μm flux observed in the off-source spectrum of Mz 3 is actually higher than that observed in the on-source spectrum (Table A1), with the emission detected in the off-source spectrum likely to be dominated by a Galactic background H II region. Given the complex structure of the emission regions in the field of Mz 3, the amount of contamination from background regions to the 158-μm flux recorded in the on-source spectrum of Mz 3 is likely to be large, so that our estimates from Fig. 6 for the temperature and density of its [C II]-emitting region can only be lower limits.

For three other nebulae plotted in Fig. 6, NGC 3918, 5189 and 6537, the net on−off [C II] 158-μm flux is smaller than the off-source value, so the temperatures and densities derived for their PDRs must be considered uncertain, and are indicated by colons in Table 5. The contamination from Galactic background emission is less severe in the case of NGC 6302. Our off-source [C II] flux, recorded 8 arcmin south and 3 arcmin west of NGC 6302, amounts to about 50 per cent of the flux recorded in our on-source spectrum. However, Castro-Carrizo et al. (2000) measured an LWS01 [C II] off-source flux 5 arcmin south of NGC 6302 that agrees well with our own, despite the two off-source measurements differing by 4.2 arcmin in position. We therefore conclude that the temperature and density estimates in Table 5 for the warm [C II]-emitting region in NGC 6302 are reasonably secure.

CPD−56°8032 and He 2-113, which both have a WC10 central star and the highest gas C/O abundance ratio known for a PN (De Marco, Barlow & Storey 1997), fall beyond the boundary of Fig. 6, well outside the 5000-K locus. The recent analysis of Cohen et al. (1999) of the 2.4–197 μm SWS and LWS spectra of

[2] Fong et al. (2001) and Castro-Carrizo et al. (2000) have used higher spectral resolution LWS Fabry-Perot spectra of these lines from PN and post-AGB objects to convincingly rule out a significant contribution from shocks to the line excitation.

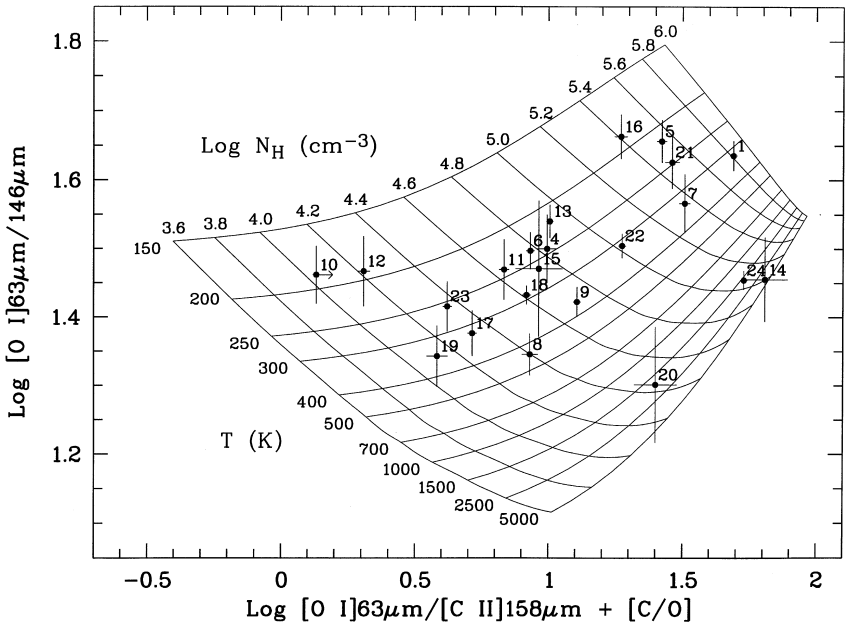

Figure 6. The PDR temperature-density plane defined by the [O I] 63 μm/146 μm line ratio and the ratio of the 63-μm line to the [C II] 158-μm line. [C/O] ≡ log(C/O) − log(C/O)$_\odot$, where (C/O)$_\odot$ = 0.5 is the cosmic C/O ratio. The grid gives calculated line intensity ratios for a range of values of T and log N_H. The data points are labelled by the nebular sequence numbers given in Table 5.

CPD−56°8032 however reveals the clear and simultaneous presence of circumstellar dust emission features from both oxygen- and carbon-rich materials, suggesting that it may have experienced a recent transition from an O-rich to a C-rich outflow following a helium flash (Cohen et al. 1999). It is thus not implausible that the gas-phase C/O abundance ratio in the PDR around CPD−56°8032 may well be significantly lower than the extremely high value of 13 deduced for the inner, ionized region by De Marco et al. (1997). If we assume a gas C/O ratio of unity for the PDR of CPD−56°8032, then the observed 63 μm/146 μm and 63 μm/158 μm ratios yield $T = 430$ K and $\log N_H = 5.2$. Similarly, for C/O = 1, we find $T = 390$ K and $\log N_H = 5.5$ for He 2-113. These values are comparable to those deduced for the PDRs of the other PN in our sample. Thus our analysis of the PDRs in CPD−56°8032 and He 2-113 lends further support to the finding of Cohen et al. that CPD−56°8032, and probably also its twin He 2-113, may have switched very recently from an O-rich outflow to a C-rich outflow.

Assuming a cosmic C/O ratio, the 63 μm/146 μm and 63 μm/158 μm ratios derived from both the on- and off-source spectra of Lo 14 (Table 2) would fall to the lower left outside Fig. 6, well below the locus of $T = 5000$ K *and* the locus of $N_H \rightarrow 0$. The abnormal line ratios cannot be explained by varying the unknown C/O abundance ratio, since varying the C/O ratio will only move a data point horizontally in Fig. 6. In Appendix B we discuss the likelihood that the emission lines detected in the on- and off-source spectra of Lo 14 are associated with the Galactic radio source G 331.5−0.1 and H II regions in the Galactic plane, respectively. The very low 63 μm/146 μm and 63 μm/158 μm ratios derived from these two spectra clearly show that the physical properties of the emitting regions are quite different from the PDRs of PN. Such low 63 μm/146 μm and 63 μm/158 μm ratios have also been found in material associated with H II regions (Baluteau et al. 1997) and pre-main-sequence stars (Lorenzetti et al. 1999) and seem to be caused by very high optical depths through those regions, such that the [O I] 63-μm line is self-absorbed. By contrast, the PDR emission lines observed from PN are generally optically thin.

Of the 22 PN plotted in Fig. 6, all except three fall in a narrow band of temperature from 200–500 K, and are split into two distinct groups in density, one near $\log N_H \sim 4.7$(cm^{-3}) and another smaller group at $\log N_H \sim 5.5$(cm^{-3}). The latter group includes the well known young dense PN BD+30°3639, IC 418, IC 5117, and NGC 5315 and 6572. Density determinations for the ionized regions of these nebulae using diagnostics with high critical densities, such as the [Ar IV] and [Cl III] optical doublet ratios, also yield high electron densities ranging from 10^4–10^5 cm^{-3} (Table 3). The electron density in the ionized region is thus approximately an order of magnitude lower than the derived density of the PDR of the same nebula. Similar differences between the densities inferred for the ionized region and the PDR are apparent for the nebulae with lower densities, which are mostly well-developed PN where a significant fraction of their envelope has been ionized. In these nebulae, the PDRs are likely to be dominated by dense knots and filaments that have survived being fully ionized by the strong radiation field from the central star.

The PDRs of three nebulae in our sample, NGC 3918, NGC 6543 and NGC 7027, show very high temperatures, 3900, 1800 K and 1600 K, respectively, well above the typical value of a few hundred K derived for other nebulae. For such high temperatures, the 63 μm/146 μm and 63 μm/158 μm ratios are however very insensitive to temperature and a small uncertainty in the observed line ratios or the assumed C/O abundance ratio can lead to a very large error in the deduced temperature. As discussed above, the net on−off [C II] flux for NGC 3918 is only a third of the off-source flux. Taking the errors in the observed line ratios at their face values, the observation of NGC 3918 could be consistent with a PDR temperature as low as 1000–1500 K. The C/O ratio of NGC 3918 is also somewhat uncertain. From detailed photoionization modelling, Clegg et al. (1987) deduced a C/O abundance ratio of 1.6 for the ionized regions of NGC 3918. For this C/O ratio,

however, the observed 63 μm/146 μm and 63 μm/158 μm ratios of NGC 3918 would fall outside to the right of the locus of $T = 5000$ K. On the other hand, from the intensity ratio of the C III] λ1908 and O III] λ1661 lines and the ratio of the λ1908 to the [O III] λ5007 line, Rola & Stasínska (1994) derived a C^{2+}/O^{2+} ionic abundance ratio of 1.15 and 0.9 respectively, comparable to the value of 0.8 deduced from the C II and O II optical recombination lines (Liu et al. 1999). Here we have adopted a C/O ratio of unity. Given these uncertainties, the very high temperature of 3900 K deduced for the PDR of NGC 3918 should be taken with great caution.

Excluding the uncertain result for NGC 3918, the PDR of NGC 7027, with $T = 1600$ K and $\log N_H \sim 5.1(\mathrm{cm}^{-3})$, is one of the warmest and *at the same time* one of the densest amongst the PN in our sample. NGC 7027 is also the only PN observed by us with the LWS where CH^+ emission has been detected (Cernicharo et al. 1997). That CH^+ could have a detectable abundance around a high excitation PN was first predicted by Black (1978). Apart from being C-rich, the strong CH^+ emission from NGC 7027 may be explainable by the extremely high temperature in its PDR, which ensures a rapid reaction rate for $C^+ + H_2 \rightarrow CH^+ + H$ (which has an activation energy of ~4000 K). Recent modelling by Yan et al. (1999) of the thermal and chemical structure of the PDR of NGC 7027 shows that the temperature in the dense shell of the PDR decreases outwards from a temperature of over 3000 K to under 200 K. The intensities of pure rotational lines of CO (from $J = 29$–28 to $J = 14$–13), CH^+, OH and CH predicted by their models are in good agreement with the LWS observations (Liu et al. 1996; Cernicharo et al. 1997; Liu et al. 1997). Yan et al. did not however predict fluxes for the [O I] and [C II] lines.

6 NEUTRAL REGION MASS ESTIMATES

The [C II] 158-μm line has a low critical density (2.7×10^3 cm^{-3} for H^0 impacts), much smaller than the densities deduced here for the PDRs. As a result, the $^2P_{1/2,3/2}$ levels of the C^+ ground term are thermalized and populated in proportion to their statistical weights. The 158-μm line flux can therefore be used to derive the masses (H plus He) of the PDRs, provided the C/H abundance

Table 5. Temperature and densities of PDRs.

No	Nebula	C/O	log C/H +12.0	*d* (kpc)	Refs	T (K)	log N_H (cm^{-3})	M_{gas}^{CII} ($M_\odot$)	M_{gas}^{CO} ($M_\odot$)
1	BD+30°3639	1.60	8.60	1.5	1,22	320	5.8	0.20	0.0027
2	CPD−56°8032	13.1	9.80	1.4	2			0.0039	0.046
3	He 2-113	10.4	9.70	1.5	2			0.0064	0.016
4	He 2-131	0.30	8.15	1.4	3,23	240	4.8	0.097	
5	IC 418	1.30	8.43	1.2	3,21,24	220	5.5	0.20	
6	IC 4406	(0.50)	8.45	3.1	14,25	240	4.8	0.85	0.043
7	IC 5117	1.39	9.75	3.8	4,15,24	330	5.4	0.026	0.039
8	IRAS 21282+5050	(0.50)	(8.55)	1.0		440	4.4	0.070:	0.043
9	M 2-9	(0.50)	8.14	1.7	16,23	360	4.7	0.61	0.0016
10	Mz 3	(0.50)	(8.55)	2.7	25	>190	>4.0	<2.4	0.0077
11	NGC 40	1.25	8.90	0.5	5,26	240	4.6	0.019	
12	NGC 2346	0.35	8.34	0.8	4,17,26	190	4.2	0.060	
13	NGC 3132	0.63	8.78	0.5	4,18,27	220	4.9	0.015	0.0090
14	NGC 3918	1.00	8.90	1.0	4,19,23	3900:	5.0:	0.0044:	
15	NGC 5189	0.34	8.12	1.5	6,25	260:	4.7:	0.060:	
16	NGC 5315	0.31	8.29	2.6	4,6,25	190	5.4	0.39	
17	NGC 6072	(0.50)	8.33	1.3	14,25	320	4.3	0.22	0.14
18	NGC 6302	0.88	8.64	1.6	7,28,29	290	4.6	0.59	0.056
19	NGC 6537	0.42	8.32	0.9	8,14,25	340:	4.1:	0.065:	
20	NGC 6543	1.20	8.88	1.9	9,24	1800	4.4	0.015	
21	NGC 6572	0.62	8.33	1.2	10,22	250	5.5	0.10	
22	NGC 6720	1.10	8.90	0.7	11,12,30	310	5.0	0.031	0.032
23	NGC 6781	(0.50)	8.34	0.7	20,23	260	4.4	0.10	0.17
24	NGC 7027	1.88	8.98	0.7	13,31	1600	5.1	0.16	0.22
	Hb 12	0.52	8.06	3.0	32,24			0.69:	
	M 2-55	(0.50)	(8.55)	2.2	23			0.17:	
	NGC 6826	0.34	8.12	1.6	12,23			0.045	
	Vy 2-2	0.30	(8.15)	4.0	24			0.83:	0.011

References: 1. Pwa, Pottasch & Mo (1986); 2. De Marco, Barlow & Storey (1997); 3. Adams & Seaton (1982); 4. Rola & Stasínska (1994); 5. Clegg et al. (1983); 6. Kingsburgh & Barlow (1994); 7. Aller et al. (1981); 8. Calculated from the line fluxes given by Feibelman et al. (1985); 9. Middlemass, Clegg & Walsh (1989); 10. Hyung, Aller & Feibelman (1994b); 11. Barker (1987); 12. Kwitter & Henry (1998); 13. Kwitter & Henry (1996); 14. Perinotto & Corradi (1998); 15. Aller & Czyzak (1983); 16. Barker (1978); 17. Peimbert & Torres-Peimbert (1987); 18. Torres-Peimbert & Peimbert (1977); 19. Clegg et al. (1987); 20. Aller & Keyes (1987); 21. Hyung, Aller & Feibelman (1994a); 22. Kawamura & Masson (1996); 23.Cahn et al. (1992); 24. Kingsburgh & Barlow (1992); 25. Kingsburgh & English (1992); 26. Acker et al. (1998); 27. Pottasch (1996); 28. Gomez, Rodriguez & Moran (1993); 29. Casassus, Roche & Barlow (2000); 30. Harris et al. (1996); 31. Hajian, Terzian & Bignell (1993); 32. Hyung & Aller (1996).

ratio is known. Assuming a He/H abundance ratio of 0.1 by number, the total gas mass of the [C II]-emitting region, in solar mass units, is given by

$$M_{\rm gas}^{\rm CII} = 7.3\times10^{-6}\left(\frac{\rm d}{1\,\rm kpc}\right)^2\left[\frac{f(158\,\mu\rm m)}{10^{-12}\rm erg\,cm^{-2}\,s^{-1}}\right]\left(\frac{\rm C}{\rm H}\right)^{-1},$$

where d is the nebular distance. The PDR masses derived using this equation are listed in column 9 of Table 5, using the nebular C/H abundance ratios and distances tabulated in columns 4 and 5.

The [C II] 158-μm line has been detected from four nebulae in our sample which lack detections of the [O I] 63-μm and/or 146-μm lines, namely the planetary nebulae Hb 12, M 2-55, NGC 6826 and Vy 2-2. Estimates for the masses of their [C II]-emitting regions are therefore provided at the end of Table 5. Since the net on–off [C II] 158-μm flux of Hb 12 is only about 50 per cent of the off-source flux, its mass estimate must be considered uncertain. No reliable C/H abundance determinations are available for M 2-55 and Vy 2-2. For M 2-55 we have assumed a solar C/H abundance ratio, while for Vy 2-2 we have adopted a similar C/H ratio to those of He 2-131 and Hb 12, which exhibit very similar low-excitation nebular spectra to that of Vy 2-2, as well as similar 10-μm silicate emission features (Aitken & Roche 1982)

Of the 28 PN for which we have derived neutral region masses from the [C II] 158-μm line, 15 of them have molecular envelope masses previously determined from millimetre observations of the CO $J = 2$–1 and/or $J = 1$–0 emission (Huggins et al. 1996). Their results, after converting to values corresponding to the distances adopted here, are listed in column 10 of Table 5. For seven of the nebulae, the derived masses of the [C II]-emitting and CO-emitting regions are comparable within a factor two. For the other eight nebulae, there are however significant differences between the nebular masses traced by the [C II] 158-μm line and by the millimetre CO emission. Except for the two extreme C-rich nebulae, CPD−56°8032 and He 2-113, the observed 158-μm line flux implies a neutral region much more massive than the molecular shell. The low values of $M_{\rm gas}^{\rm CII}$ deduced for CPD−56°8032 and He 2-113, smaller by factors of 12 and 3 compared to the corresponding $M_{\rm gas}^{\rm CO}$, can partly be attributed to our use of the very high C/H abundance ratios deduced for the ionized regions of these two nebulae by De Marco et al. (1997), whereas Huggins et al. (1996) adopted a constant CO abundance of 3×10^{-4} relative to H nuclei for all nebulae in their sample when converting the observed CO emission fluxes to gas masses.[3] As discussed earlier, the actual gas phase C/O abundance ratio in the PDRs of these two nebulae could be lower than those found in the ionized regions. If we assume a gas phase abundance ratio of C/O = 1 for the PDRs of both nebulae, then the neutral region masses derived for them would increase by factors of 13 and 10 respectively, relative to those listed in Table 5.

Of the three Type-I PN in our sample: Mz 3, and NGC 6302 and 6537, only NGC 6302 can be considered to have a reliable [C II] flux. The derived mass for its [C II] emitting region, 0.59 $M_\odot$, is a factor of 10 higher than the mass of the cool molecular envelope of NGC 6302 traced by millimetre CO emission (Huggins et al. 1996). By contrast, the [C II]-emitting regions of the non-Type-I PN, except for a few young dense nebulae, such as BD+30°3639, IC 418, M 2–9, NGC 5315 and 7027, all have a relatively small mass, $M_{\rm gas}^{\rm CII} \lesssim 0.1\,M_\odot$, i.e. smaller than the typical mass of 0.3–0.5 $M_\odot$ of the ionized regions of PN. Two interesting exceptions are IC 4406 and NGC 6072, with $M_{\rm gas}^{\rm CII} = 0.85$ and 0.22 $M_\odot$, respectively. Both are large, well evolved nebulae with a hot, low luminosity central star. The very high PDR mass of IC 4406 is consistent with its very strong near-IR H_2 rovibrational emission (Storey 1984). One possible scenario for the presence of such massive [C II]-emitting regions around these old PN is that following the rapid decline of the central star luminosity at late stages, the high ionization degree of the nebula can no longer be maintained and the nebula has started to recombine, leading also to a rapid formation of molecular hydrogen via the associative ionization reaction $H(n = 2) + H \rightarrow H_2^+ + e^-$ (Rawlings, Drew & Barlow 1993).

For the young, high electron density nebula BD + 30°3639, our derived [C II] emitting region mass of 0.2 $M_\odot$ is a factor of 75 higher than the mass derived for its CO envelope by Huggins et al., suggesting that most of its molecular envelope has been dissociated. Another young PN with similar properties is IC 418, which has long been known to have an extended H I emitting envelope (Taylor, Gussie & Goss 1989), yet has eluded detection in the millimetre-wave CO lines (e.g. Huggins et al. 1996). Both of these low-excitation PN have relatively cool central stars, emitting the majority of their luminosity longwards of the Lyman limit, so that CO molecules would be subjected to a strongly dissociating 912–1100 Å stellar radiation field.

7 CONCLUSIONS

The *ISO* LWS observations reported in this paper significantly improve the available data on fine-structure lines in PNe, and together with optical data have allowed us to determine the electron densities and ionic abundances in the ionized regions as well as the temperature, densities and gas masses of the associated PDRs. The main conclusions of the present study are as follows.

(1) The electron densities deduced from the [O III] 52 μm/88 μm line ratio for 21 PNe are found to be systematically lower than the densities derived from the optical doublet ratios of [Ar IV] and [Cl III], with a clear tendency for the discrepancies to become larger for higher densities. For the far-infrared lines, the derived electron densities range from 100 $\rm cm^{-3}$ to $1.2\times10^4\,\rm cm^{-3}$ while for the optical lines the derived electron densities are in the range 400 $\rm cm^{-3}$ to $6\times10^4\,\rm cm^{-3}$. This trend is interpreted as being due to the effects of density inhomogeneities in the nebulae rather than a consequence of temperature fluctuations.

(2) The ionic abundances N^+/H^+, N^{2+}/H^+, and O^{2+}/H^+ have been derived using the electron density derived from the [O III] 52 μm/88 μm line ratio. The N^{2+}/O^{2+} abundance ratio, which provides a good approximation to the N/O elemental abundance ratio irrespective of the adopted electron density, covers a wide range, from 0.10 (i.e. close to the solar value of 0.12), to the extreme value of 2.03 found in the PN Mz 3.

(3) The temperature and densities of the associated PDRs have been estimated from the [C II] and [O I] fine-structure lines for 24 PNe. The deduced temperatures fall between 200 and 500 K, and the densities vary from $10^4\,\rm cm^{-3}$ to $3\times10^5\,\rm cm^{-3}$. The young PN NGC 7027 is outstanding for its warm (1600 K) and dense ($10^5\,\rm cm^{-3}$) PDR. Except in a few sources, the masses associated

[3] In general, the CO-emitting region mass estimates of Huggins et al. are unlikely to be greatly in error even when the actual nebular C/H ratio exceeds their adopted CO/H ratio of 3×10^{-4}, since the almost invariant O/H abundance ratio of 5×10^{-4} found for galactic PN (Kingsburgh & Barlow 1994) places a firm upper limit of 5×10^{-4} on the CO/H nucleus ratio in the neutral zone.

with the PDRs in PN are generally modest and do not exceed $0.1\,M_{\odot}$.

These *ISO* LWS observations of PN have highlighted the importance of the far-infrared fine-structure lines for studying the physical conditions and deriving the abundances in these objects. The fine-structure lines are found generally to be strong and it is clear that future infrared facilities will provide key opportunities to investigate further the far-infrared properties of PN. In particular, the airborne facility SOFIA will allow one to observe the fine-structure lines from planetary nebula PDRs using a better angular and spectral resolution than was possible with *ISO*. The satellite *FIRST* with its imaging and spectral capabilities will also be able to study the far-infrared fine-structure emission lines and to map their distribution for the more extended PN. These future perspectives will provide the opportunity to develop a complete picture of the evolution of PN by providing information on the atomic and ionized components that will complement and enhance existing ground based optical studies and molecular observations.

REFERENCES

Acker A., Fresneau A., Pottasch S. R., Jasniewicz G. J., 1998, A&A, 337, 253
Acker A., Ochsenbein F., Stenholm B., Tylenda R., Marcout J., Schohn C., 1992, Strasbourg–ESO catalogue of Galactic Planetary Nebulae. ESO, Garching
Adams S., Seaton M. J., 1982, MNRAS, 200, 7
Aggarwal K. M., 1983, ApJS, 52, 387
Aitken D. K., Roche P. F., 1982, MNRAS, 200, 217
Aller L. H., Czyzak S. J., 1979, Ap&SS, 62, 397
Aller L. H., Czyzak S. J., 1983, ApJS, 51, 211
Aller L. H., Keyes C. D., 1987, ApJS, 65, 405
Aller L. H., Ross J. E., O'Mara B. J., Keyes C. D., 1981, MNRAS, 197, 95
Amaral L. H., Abraham Z., 1991, A&A, 251, 259
Anders E., Grevesse N., 1989, Geochim. Cosmochim. Acta, 53, 197
Baluja K. L., Zeippen C. J., 1988, J. Phys. B., 21, 1455
Baluteau J. P., Joubert M., Cox P., Caux E., Emery R., 1997, in Kessler M. F., eds, ESA SP-419, The First *ISO* Workshop on Analytical Spectroscopy. ESA Publications, Noordwijk, p. 99
Barker T., 1978, ApJ, 220, 193
Barker T., 1987, ApJ, 322, 922
Black J. H., 1978, ApJ, 222, 125
Blum R., Pradhan A. K., 1992, ApJS, 80, 425
Butler K., Zeippen C. J., 1989, A&A, 208, 337
Cahn J. H., Kaler J. B., Stanghellini L., 1992, A&AS, 94, 399
Casassus S., Roche P. F., Barlow M. J., 2000, MNRAS, 314, 657
Castro-Carrizo A., Bujarrabal V., Fong D., Meixner M., Tielens A. G. G. M., Alcolea J., Trams N., 2000, A&A, 368, 34
Cernicharo J., Liu X.-W., Gonzalez-Alfonso E., Cox P., Barlow M. J., Lim T., Swinyard B. M., 1997, ApJ, 483, L65
Clegg P. E. et al., 1996, A&A, 315, L38
Clegg R. E. S., Seaton M. J., Peimbert M., Torres-Peimbert S., 1983, MNRAS, 205, 417
Clegg R. E. S., Harrington J. P., Barlow M. J., Walsh J. R., 1987, ApJ, 314, 551
Cohen M., 1975, PASP, 87, 500
Cohen M., Barlow M. J., Sylvester R., Liu X.-W., Cox P., Schmidt B. S., Speck A. K., 1999, ApJ, 513, L135
Condon J. J., Griffith M. R., Marks R., Wright A. E., 1993, AJ, 106, 1095
de Graauw Th., Haser L. N., Beintema D. A., 1996, A&A, 315, L49
De Marco O., Barlow M. J., Storey P. J., 1997, MNRAS, 292, 86
Dinerstein H. L., Haas M. R., Erickson E. F., Werner M. W., 1995, in Haas M. R., Davidson J. A., Erickson E. F., eds, Airborne Astronomy Symp. on the Galactic Ecosystem. Astron. Soc. Pac., San Francisco, p. 387 (see N96-13618 02-88)
Dinerstein H. L., Lester D., Werner M. W., 1985, ApJ, 291, 561
Ellis H. B., Werner M. W., 1984, BAAS, 16, 463
Fang Z., Kwong H. S., Parkinson W. H., 1993, ApJ, 413, L141
Feibelman W. A., Aller L. H., Keyes C. D., Czyzak S. J., 1985, Proc. Natl. Acad. Sci., USA, 82, 2202
Fong D., Meixner M., Castro-Carrizo A., Bujarrabal V., Latter W., Kelly D., Sutton E., 2001, A&A, 367, 652
French H. B., 1981, ApJ, 246, 434
Gomez Y., Rodriguez L. F., Moran J. M., 1993, ApJ, 416, 620
Grevesse N., Noels A., 1993, in Prantzos N., Vangioni-Flam E., Cassé M., eds, Origin and Evolution of the Elements. Cambridge Univ. Press, Cambridge, p. 15
Hazard C., Terlevich R., Morton D. C., Sargent W. L. W., Ferland G., 1980, Nat, 285, 463
Hajian A. R., Terzian Y., Bignell C., 1993, AJ, 106, 1965
Harris H. C., Dahn C. C., Monet D. G., Pier J. R., 1997, in Habing H. J., Lamers H. J. G. L. M., eds, Planetary Nebulae. Kluwer, Dordrecht, p. 40
Herbst W., 1975, AJ, 80, 212
Huggins P. J., Bachiller R., Cox P., Forveiller T., 1996, A&A, 315, 284
Hyung S., Aller L. H., 1996, MNRAS, 278, 551
Hyung S., Aller L. H., Feibelman W. A., 1994a, PASP, 106, 745
Hyung S., Aller L. H., Feibelman W. A., 1994b, MNRAS, 269, 975
Hyung S., Keyes C. D., Aller L. H., 1995, MNRAS, 272, 49
Jacoby G. H., 1979, PASP, 91, 574
Jacoby G. H., Ford H. C., 1983, ApJ, 266, 298
Kawamura J., Masson C., 1996, ApJ, 461, 282
Keenan F. P., Lennon D. J., Johnson C. T., Kingston A. E., 1986, MNRAS, 220, 571
Keenan F. P., McKenna F. C., Bell K. L., Ramsbottom C. A., Wickstead A. W., Aller L. H., Hyung S., 1997, ApJ, 487, 457
Kessler M. F. et al., 1996, A&A, 315, L27
Kingsburgh R. L., Barlow M. J., 1992, MNRAS, 257, 317
Kingsburgh R. L., Barlow M. J., 1994, MNRAS, 271, 257
Kingsburgh R. L., English J., 1992, MNRAS, 259, 635
Kwitter K. B., Henry R. B. C., 1996, ApJ, 473, 304
Kwitter K. B., Henry R. B. C., 1998, ApJ, 493, 247
Launay J.-M., Roueff E., 1977a, J. Phys. B, 10, 879
Launay J.-M., Roueff E., 1977b, A&A, 56, 289
Lennon D. J., Burke V. M., 1994, A&AS, 103, 273
Lim T., Swinyard B. M., Liu X. W., Burgdorf M., Gry C., Pezzuto S., Tommasi E., 1997, in Kessler M. F., eds, ESA SP-419, The First *ISO* Workshop on Analytical Spectroscopy. ESA Publications, Noordwijk, p. 281
Liu X. W., 1997, in Kessler M. F., eds, ESA SP-419, The First *ISO* Workshop on Analytical Spectroscopy. ESA Publications, Noordwijk, p. 87
Liu X.-W. et al., 1996, A&A, 315, L257
Liu X.-W. et al., 1997, MNRAS, 290, L71
Liu X.-W., Danziger I. J., 1993, MNRAS, 263, 256
Liu X.-W., Storey P. J., Barlow M. J., Danziger I. J., 1999, in Walsh J. R., Rosa M. R., eds, Chemical Evolution from Zero to High Redshift. Springer-Verlag, Berlin, p. 39
Liu X.-W., Storey P. J., Barlow M. J., Danziger I. J., Cohen M., Bryce M., 2000b, MNRAS, 312, 585
Longmore A. J., 1977, MNRAS, 178, 251
Lorenzetti D. et al., 1999, A&A, 346, 604
Melnick G., Russell R. W., Gull G. E., Harwit M., 1981, ApJ, 243, L35
Mendoza C., Zeippen C. J., 1982, MNRAS, 198, 127
Middlemass D., Clegg R. E. S., Walsh J. R., 1989, MNRAS, 239, 1
Nussbaumer H., Rusca C., 1979, A&A, 72, 129
Nussbaumer H., Storey P. J., 1981a, A&A, 99, 177
Nussbaumer H., Storey P. J., 1981b, A&A, 96, 91
Peimbert M., 1967, ApJ, 150, 825
Peimbert M., 1971, Bol. Obs. Tonantzintla y Tacubaya, 6, 29
Peimbert M., Torres-Peimbert S., 1983, in Flower D. R., eds, Planetary Nebulae. Kluwer, Dordrecht, p. 233
Peimbert M., Torres-Peimbert S., 1987, Rev. Mex. Astron. Astrofis., 14, 540

Péquignot D., 1990, A&A, 231, 499
Péquignot D., 1996, A&A, 313, 1026
Perinotto M., Corradi R. L. M., 1998, A&A, 332, 721
Pottasch S. R., 1996, A&A, 307, 561
Pwa T. H., Pottasch S. R., Mo J. E., 1986, 164, 184
Ramsbottom C. A., Bell K. L., Keenan F. P., 1997, MNRAS, 284, 754
Rawlings J. M. C., Drew J. E., Barlow M. J., 1993, MNRAS, 265, 968
Rola C., Stasínska G., 1994, A&A, 282, 199
Rubin R. H., 1989, ApJS, 69, 897
Rubin R. H., Colgan S. W. J., Haas M. R., Lord S., Simpson J. P., 1997, ApJ, 479, 332
Stafford R. P., Bell K. L., Hibbert A., Wijesundera W. P., 1994, MNRAS, 268, 816
Storey J. W. V., 1984, MNRAS, 206, 521
Storey P. J., Hummer D. G., 1995, MNRAS, 272, 41
Swinyard B. M. et al., 1996, A&A, 315, L43
Taylor A. R., Gussie G. T., Goss W. M., 1989, ApJ, 340, 932
Torres-Peimbert S., Peimbert M., 1977, Rev. Mex. Astron. Astrofis., 2, 181
van den Bergh S., Herbst W., 1975, AJ, 80, 208
Viegas S., Clegg R. E. S., 1994, MNRAS, 271, 993
Watson D. M., 1983, in Kessler M. F., Phillips J. P., eds, Galactic & Extragalactic Infrared Spectroscopy. ESA Special Publication, Noordwijk, p. 193
Wheelock S. et al., 1994, in *IRAS* Sky Survey Atlas Explanatory Supplement, JPL Publication 94-11, Pasadena
Yan M., Federamn S. R., Dalgarno A., Bjorkman J. E., 1999, ApJ, 515, 640
Zeippen C. J., Butler K., Le Bourlot J., 1987, A&A, 188, 251

APPENDIX A: LINE FLUXES FROM INDIVIDUAL SPECTRA AND DETECTORS

In Table A1 we present the fluxes measured from the individual LWS detector sub-spectra for a variety of infrared fine structure lines, for both on-source and (when they were acquired) off-source spectra of each target. The 'on–off' fluxes represent the fluxes measured from net spectra after subtraction of the off-source spectrum from the on-source spectrum, and so may differ from the difference between the fluxes measured on the individual on-source and off-source spectra.

APPENDIX B: LO 14 AND MZ 3

B1 Lo 14

Lo 14 was identified as a possible PN candidate by Longmore (1977), from the presence of a surrounding nebulosity on UK Schmidt plates. However, this nebulosity had previously been classified as a reflection nebula (vdBH 69) by van den Bergh & Herbst (1975). Herbst (1975) obtained UBV photometry and an MK spectral type of M6:III: for the V = 11.27 star CD−50°10202 that is located very close to vdBH69/Lo 14. He found the star to be variable (with a range of 0.34 mag over 6 measurements) and estimated $E(B–V) = 0.69$ and a distance modulus m–M of approximately 9.8 magnitudes. No optical emission lines have ever been found at the coordinates of Lo 14, $\alpha(2000) = 16^{\rm h}11^{\rm m}44\overset{\rm s}{.}9$ and $\delta(2000) = -51°17'54''$, and so the object was rejected as a planetary nebula in the Strasbourg PN catalogue of Acker et al. (1992). Our own 3200–7400 Å AAT spectrum shows no nebular emission lines within ±10 arcsec of CD−50°10202 along an EW slit through the star. The *IRAS* Point Source Catalog lists a strong infrared source at the position of CD−50°10202, IRAS 16079−5110, with fluxes of 93.5, 61.3 and 170 Jy at 12, 25 and 60 μm. Since the variability of the M giant star, the presence of reflection nebulosity and strong apparent infrared dust emission appeared to indicate a highly evolved AGB object, we included this object in a sample, the far-IR dust continuum emission of which was to be investigated via LWS grating spectra. We were therefore surprised to detect far-IR ionic fine structure emission lines in our *ISO* spectra, superposed on a strong continuum. The LWS on-source and off-source spectra of Lo 14, respectively taken centred on CD−50°10202 and at a position 627 arcsec west and 25 arcsec north of Lo 14, show strong emission in the [N III] 57-μm and [O III] 52- and 88-μm lines. The lack of detectable optical line emission at the position of CD−50°10202 suggests that the far-IR emission line source is heavily obscured. However, it would be of interest to obtain deep optical spectra of the nebulosity that is visible on the ESO R-plate ∼45 arcsec to the northeast of CD−50°10202.

Inspection of the Parkes–MIT–NRAO (PMN) 4850-MHz map of the field (Condon et al. 1993) suggests that the emission lines detected in the LWS spectra might be associated with a nearby bright thermal radio source G 331−0.1 [$\alpha(2000) = 16^{\rm h}12^{\rm m}11^{\rm s}$, $\delta(2000) = -51°26'54''$; Amaral & Abraham 1991], about 10 arcmin from the LWS on-source aperture centre. The *IRAS* 60- and 100-μm atlases show that G 331−0.1 is also a very strong infrared source, its coordinates coincide with the extremely bright far-IR source IRAS 16086 − 5119 [$\alpha(2000) = 16^{\rm h}12^{\rm m}24^{\rm s}$, $\delta(2000) = -51°27'29''$]. On the *IRAS* 60- and 100-μm atlases as well as the PMN 4850-MHz map of the field, apart from the bright source at the position of G 331.5−0.1 and IRAS 16086−5119, strong diffuse emission is seen along the Galactic plane. An abundance analysis (Section 4) of the LWS spectrum taken centred on the position of Lo 14 yields a high N^{2+}/O^{2+} abundance ratio of 0.6, suggesting that the emission arises from highly chemically processed material. On the other hand, the off-source LWS spectrum of Lo 14 yields a solar-like N/O ratio of 0.12, suggesting that the emission detected in this spectrum arises from diffuse H II regions in the Galactic plane. Given the uncertain nature of the emission detected in the LWS on- and off-source spectra of Lo 14, the fluxes derived from the two spectra are listed separately in Table 2, under the headings of 'Lo 14 on-source' and 'Lo 14 off-source', and no background-subtracted fluxes are given.

B2 Mz 3

Mz 3 is a young low excitation PN (Cohen 1975). Its LWS off-source spectrum, taken 400 arcsec west and 301 arcsec south of Mz 3, shows the [O III] 88-μm line, in addition to the three [O I] and [C II] neutral region lines. Inspection of the PMN 4850-MHz map of the field shows a number of patchy emission regions, with Mz 3 (PK 331−01°1) falling on the west edge of one of the brighter ones of approximately 15 arcmin by 30 arcmin size at PA = 60°. The aperture of the LWS off-source spectrum of Mz 3 unfortunately fell on this bright H II region, explaining the presence of the 88-μm line in the spectrum. There is a weak but clear drop in surface brightness on the 4850-MHz map between the H II region and Mz 3, suggesting that contamination from the H II region of the on-source ionized nebular line spectrum of Mz 3 is probably not serious. We have thus adopted the fluxes measured from the on-source spectrum without background subtraction. Line fluxes from the off-source spectrum are listed separately in Table 2. We note however, that the off-source [C II] 158-μm flux measured near Mz 3 is actually larger than the flux measured on-source, so that we only have an upper limit on the true [C II] 158-μm flux from Mz 3.

Table A1. *ISO* LWS fine-structure line fluxes of planetary nebulae.

Source	[N II] 122 μm	[N III] 57 μm		[O III] 52 μm		[O III] 88 μm		[O I] 63 μm		[O I] 146 μm		[C II] 157 μm	
	LW2	SW2	SW3	SW1	SW2	SW5	LW1	SW2	SW3	LW3	LW4	LW3	LW4
BD +30 3639	0.73 ± 0.12	<3.76	<2.16	<17.1	<6.06	<1.37	<3.02	75.9 ± 3.12	70.8 ± 2.60	1.62 ± 0.08	1.95 ± 0.16	4.61 ± 0.12	4.92 ± 0.11
CPD −56 8032	<0.37	<3.66	<2.31	<22.4	<4.54	<1.76	<2.16	27.1 ± 1.68	28.2 ± 1.35	0.84 ± 0.09	0.87 ± 0.08	1.69 ± 0.09	1.73 ± 0.09
Cn 1-5 on	0.25 ± 0.06	11.6 ± 0.95	12.6 ± 0.75	25.9 ± 2.37	21.4 ± 1.94	8.07 ± 0.66	8.47 ± 0.47	2.60 ± 1.29	2.40 ± 0.40	0.13 ± 0.04	0.27 ± 0.05	0.78 ± 0.12	0.71 ± 0.05
Cn 1-5 off	<0.17	<2.82	<1.55	<10.6	<4.08	<1.35	<1.14	<3.51	<0.81	<0.21	<0.32	0.44 ± 0.08	0.62 ± 0.10
Cn 1-5 on-off	<0.24	12.0 ± 1.86	12.0 ± 0.86	26.4 ± 3.89	22.8 ± 2.51	8.40 ± 0.94	8.36 ± 0.52	3.44 ± 0.68	2.15 ± 0.53	<0.24	<0.51	<0.37	<0.41
Hb 12 on	<0.26	<2.49	<1.23	<10.2	<3.54	<1.46	1.10 ± 0.30	7.34 ± 0.77	7.30 ± 0.70	0.12 ± 0.05	–	3.80 ± 0.16	4.30 ± 0.14
Hb 12 off	<0.25	<2.51	<2.93	<19.6	<3.54	<1.89	<1.09	<3.27	0.86 ± 0.23	<0.19	<0.18	2.64 ± 0.12	3.02 ± 0.12
Hb 12 on-off	<0.37	<3.57	<4.51	<22.6	<5.34	<2.57	<1.41	5.68 ± 1.25	6.30 ± 0.76	<0.29	–	1.11 ± 0.14	1.31 ± 0.16
He 2-113 on (R079)	<0.22	<3.61	<1.97	<14.0	<5.31	<1.93	<0.82	43.9 ± 2.78	44.9 ± 1.61	0.91 ± 0.08	1.20 ± 0.05	2.51 ± 0.22	2.76 ± 0.12
He 2-113 on (R669)	<0.54	<2.47	<1.94	<16.4	<3.81	<1.44	<0.92	43.7 ± 1.93	43.3 ± 1.49	1.29 ± 0.07	1.50 ± 0.10	3.23 ± 0.15	3.51 ± 0.10
He 2-113 on (av)	<0.12	<0.78	<0.48	<4.05	<1.19	<0.44	<0.22	44.5 ± 1.85	44.1 ± 1.50	1.14 ± 0.06	1.36 ± 0.06	2.94 ± 0.10	3.25 ± 0.08
He 2-113 off (R079)	<0.15	<4.57	<1.28	<7.01	<6.61	<1.31	<0.78	<3.70	1.08 ± 0.29	<0.12	<0.22	1.22 ± 0.10	1.18 ± 0.08
He 2-113 on-off (R079)	<0.28	<5.99	<2.36	<15.5	<8.61	<2.40	<1.21	42.7 ± 2.65	43.7 ± 1.67	0.70 ± 0.09	1.10 ± 0.09	1.23 ± 0.22	1.55 ± 0.12
He 2-113 on-off (R669)	<0.56	<5.20	<2.35	<17.5	<7.38	<1.99	<1.24	42.5 ± 2.05	42.3 ± 1.54	1.16 ± 0.08	1.45 ± 0.10	1.97 ± 0.18	2.29 ± 0.10
He 2-113 on-off (av)	<0.20	<4.64	<1.38	<7.77	<6.59	<1.39	<0.84	42.9 ± 1.98	43.1 ± 1.55	1.02 ± 0.08	1.27 ± 0.09	1.70 ± 0.13	2.05 ± 0.09
He 2-131	0.50 ± 0.17	<3.90	<4.11	<11.2	<5.48	<2.20	<2.21	17.0 ± 1.87	15.5 ± 1.01	0.52 ± 0.06	0.43 ± 0.11	0.77 ± 0.07	1.26 ± 0.09
HD 44179 on	<0.29	<1.92	<0.98	<13.4	<2.69	<1.19	<0.65	2.30 ± 0.63	2.17 ± 0.24	<0.21	<0.16	0.51 ± 0.05	0.64 ± 0.07
HD 44179 off	<0.20	<2.19	<1.42	<8.63	<2.82	<1.95	<0.91	<2.92	<0.74	<0.11	<0.22	0.38 ± 0.06	0.39 ± 0.13
HD 44179 on-off	<0.37	<2.85	<1.73	<16.6	<3.88	<2.40	<1.17	5.40 ± 1.10	2.49 ± 0.37	<0.25	<0.27	<0.39	<0.31
Hu 2-1		<4.42			9.04 ± 2.14		1.53 ± 0.50						
IC 418 on (R689)	1.05 ± 0.06	18.0 ± 1.00	16.3 ± 0.66	83.1 ± 3.76	77.1 ± 3.72	12.2 ± 0.57	13.7 ± 0.71	56.9 ± 2.61	52.6 ± 2.07	1.23 ± 0.06	1.53 ± 0.12	–	–
IC 418 on (R868)	0.99 ± 0.05	16.2 ± 0.95	16.7 ± 0.87	84.7 ± 3.64	74.2 ± 2.96	13.3 ± 0.64	13.9 ± 0.65	53.4 ± 2.15	52.4 ± 2.14	1.33 ± 0.04	1.63 ± 0.05	5.61 ± 0.11	6.06 ± 0.14
IC 418 on (av)	1.04 ± 0.05	17.3 ± 0.90	16.3 ± 0.65	84.2 ± 3.13	75.6 ± 3.09	13.0 ± 0.56	13.9 ± 0.68	55.1 ± 2.25	52.2 ± 2.08	1.28 ± 0.03	1.56 ± 0.07	5.61 ± 0.11	6.06 ± 0.14
IC 418 off (R689)	<0.25	<2.98	<2.09	<11.2	<3.62	<1.66	<1.22	<2.38	<1.35	<0.16	<0.48	–	–
IC 418 off (R868)	<0.20	<3.36	<1.64	<10.3	<3.70	<1.99	<1.23	<3.19	<0.73	<0.21	<0.69	0.67 ± 0.16	0.61 ± 0.10
IC 418 off (av)	0.19 ± 0.07	<1.16	<0.62	<4.03	<1.39	<0.64	<0.43	<0.98	<0.37	<0.06	<0.22	0.67 ± 0.16	0.61 ± 0.10
IC 418 on-off (R689)	1.00 ± 0.08	18.5 ± 1.63	15.6 ± 1.03	84.8 ± 5.07	75.4 ± 3.91	11.6 ± 0.73	12.3 ± 0.83	55.3 ± 2.47	52.3 ± 1.99	1.06 ± 0.06	1.50 ± 0.20	–	–
IC 418 on-off (868)	0.63 ± 0.08	16.9 ± 1.55	15.8 ± 0.98	70.1 ± 8.87	75.0 ± 3.44	13.3 ± 0.96	13.9 ± 0.68	53.1 ± 2.46	51.7 ± 2.19	1.46 ± 0.12	1.38 ± 0.18	4.93 ± 0.17	5.44 ± 0.18
IC 418 on-off (av)	0.84 ± 0.06	18.6 ± 1.27	15.8 ± 0.82	82.2 ± 5.79	75.1 ± 3.21	12.6 ± 0.67	13.2 ± 0.69	54.5 ± 2.37	51.8 ± 2.03	1.14 ± 0.07	1.39 ± 0.19	4.93 ± 0.17	5.44 ± 0.18
IC 3568 (R213)	<0.19	4.19 ± 1.65	5.04 ± 0.53	41.5 ± 2.06	36.6 ± 2.25	19.4 ± 0.99	19.6 ± 0.91	<2.48	<0.75	<0.07	<0.18	<0.24	<0.15
IC 3568 (R717)	<0.18	7.33 ± 1.10	5.97 ± 0.57	37.2 ± 2.45	37.1 ± 2.00	18.6 ± 0.73	19.6 ± 0.74	<1.98	<0.84	<0.10	<0.20	<0.23	<0.18
IC 3568 (av)	0.12 ± 0.04	6.20 ± 0.94	5.89 ± 0.49	38.9 ± 1.79	37.2 ± 1.73	18.9 ± 0.70	19.9 ± 0.67	<0.58	<0.23	<0.03	<0.06	<0.17	<0.05
IC 4191		5.14 ± 2.43			48.5 ± 3.74		13.3 ± 0.87						
IC 4634		<3.41			36.4 ± 2.20		11.1 ± 0.59						
IC 4406	1.29 ± 0.14	27.0 ± 1.63	23.9 ± 1.48	93.0 ± 3.96	91.0 ± 3.48	51.7 ± 1.28	50.5 ± 1.54	28.5 ± 2.04	29.3 ± 0.97	0.88 ± 0.06	1.13 ± 0.12	3.32 ± 0.09	3.50 ± 0.09
IC 4997 on	<0.20	<2.57	<1.21	<10.7	<3.46	<1.48	0.47 ± 0.16	4.83 ± 0.97	4.08 ± 0.32	<0.15	<0.25	<0.19	<0.17
IC 4997 off	<0.15	<2.87	<1.88	<6.34	<4.32	<1.67	<1.11	<2.78	<1.00	<0.09	<0.20	<0.16	<0.22
IC 4997 on-off	<0.25	<3.91	<2.28	<13.1	<5.55	<2.32	<1.41	5.74 ± 1.59	4.55 ± 0.42	<0.19	<0.31	<0.27	<0.29
IC 5117	<0.18	<3.45	<0.96	10.0 ± 2.02	5.84 ± 1.23	<1.55	1.09 ± 0.28	16.3 ± 1.16	16.2 ± 0.63	0.38 ± 0.05	0.57 ± 0.07	1.39 ± 0.09	1.40 ± 0.05
IRAS 18059 on	<0.32	<3.27	<1.55	<6.49	<3.93	<1.89	<1.22	<2.21	<1.06	<0.30	<0.27	1.66 ± 0.16	1.66 ± 0.34
IRAS 21282 on	<0.21	<2.71	<1.37	<9.12	<4.35	<1.89	<1.06	32.0 ± 1.55	28.5 ± 1.28	1.11 ± 0.07	1.30 ± 0.11	5.99 ± 0.20	7.01 ± 0.32
IRAS 21282 off	<0.21	<3.70	<1.55	<9.50	<4.27	<1.35	<0.98	<2.36	0.82 ± 0.15	<0.25	<0.26	2.57 ± 0.19	3.16 ± 0.13
IRAS 21282 on-off	<0.31	<4.85	<2.15	<13.8	<6.39	<2.39	<1.51	32.3 ± 1.69	27.4 ± 1.41	1.14 ± 0.14	1.39 ± 0.10	3.37 ± 0.20	3.45 ± 0.32

Table A1 – *continued*

Source	[N II] 122 μm	[N III] 57 μm		[O III] 52 μm		[O III] 88 μm		[O I] 63 μm		[O I] 146 μm		[C II] 157 μm	
	LW2	SW2	SW3	SW1	SW2	SW5	LW1	SW2	SW3	LW3	LW4	LW3	LW4
Lo 14 on	42.6 ± 0.95	48.0 ± 2.12	50.9 ± 1.64	33.7 ± 5.78	36.5 ± 1.55	61.4 ± 1.51	60.2 ± 2.11	32.8 ± 1.08	29.5 ± 0.64	2.07 ± 0.46	5.59 ± 0.32	116. ± 1.77	115. ± 1.23
Lo 14 off	9.67 ± 0.28	3.99 ± 1.06	3.60 ± 0.44	<6.77	<4.51	12.3 ± 0.94	11.1 ± 1.27	11.7 ± 1.55	9.94 ± 0.28	<0.80	1.60 ± 0.27	44.8 ± 0.66	48.3 ± 0.85
Lo 14 on-off	35.6 ± 0.83	42.4 ± 2.39	46.8 ± 1.62	36.1 ± 4.70	33.9 ± 2.54	49.0 ± 1.58	49.4 ± 1.51	21.5 ± 1.58	19.4 ± 0.75	<1.76	4.05 ± 0.35	71.7 ± 1.42	66.6 ± 0.69
M 1-42 on	1.10 ± 0.17	28.3 ± 1.23	28.7 ± 1.67	38.1 ± 2.24	39.2 ± 1.99	18.4 ± 0.76	19.0 ± 0.85	5.01 ± 0.69	3.76 ± 0.25	<0.77	<1.56	2.54 ± 0.10	2.46 ± 0.36
M 1-42 off	<0.29	<2.50	<2.08	<11.5	<3.79	<1.90	<0.99	<2.44	<1.39	<0.27	<0.76	2.30 ± 0.20	1.64 ± 0.18
M 1-42 on-off	<0.89	28.6 ± 1.74	28.2 ± 1.73	37.2 ± 6.19	40.8 ± 2.45	17.0 ± 1.06	18.7 ± 0.88	4.77 ± 1.08	2.61 ± 0.43	<0.85	<1.80	<0.61	<1.81
M 1-92 on	<0.51	<3.39	<2.33	<6.29	<4.95	<1.53	<1.27	4.04 ± 1.73	3.38 ± 0.41	<0.17	<0.32	0.62 ± 0.05	0.84 ± 0.18
M 1-92 off	<0.14	<3.30	<1.31	<9.00	<4.03	<1.44	<1.22	<2.62	<0.88	<0.11	<0.24	0.68 ± 0.08	0.70 ± 0.09
M 1-92 on-off	<0.54	<5.11	<2.69	<11.6	<6.48	<2.24	<1.79	<4.14	2.97 ± 0.47	<0.21	<0.40	<0.51	<0.42
M 2-36 on	0.20 ± 0.05	4.98 ± 0.86	6.14 ± 0.54	24.4 ± 3.57	21.5 ± 1.91	7.67 ± 0.66	7.03 ± 0.52	<2.17	2.77 ± 0.29	0.17 ± 0.05	<0.21	1.14 ± 0.08	1.14 ± 0.07
M 2-36 off	<0.23	<2.43	<1.74	<6.77	<4.48	<1.77	<1.29	<3.92	<0.86	<0.15	<0.36	0.90 ± 0.23	0.87 ± 0.14
M 2-36 on-off	<0.29	<3.29	6.29 ± 0.61	26.4 ± 4.49	20.0 ± 2.76	8.85 ± 1.15	6.88 ± 0.87	<4.68	1.98 ± 0.24	<0.19	<0.36	<0.46	<0.34
M 2-55	0.86 ± 0.09	7.75 ± 1.07	9.44 ± 0.55	22.6 ± 3.27	21.1 ± 1.58	26.7 ± 1.81	25.9 ± 0.73	4.22 ± 1.02	4.93 ± 0.54	<0.21	<0.26	2.07 ± 0.19	1.46 ± 0.17
M 2-56 on	<0.24	<2.06	<1.85	<9.43	<4.16	<2.05	<1.12	<4.16	1.82 ± 0.49	<0.20	<0.24	0.83 ± 0.21	1.11 ± 0.14
M 2-56 off	<0.20	<3.22	<1.68	<12.8	<3.61	<1.54	<0.99	<2.58	2.42 ± 0.42	<0.12	<0.18	0.48 ± 0.07	0.52 ± 0.11
M 2-56 on-off	<0.31	<3.68	<2.39	<16.5	<6.00	<2.74	<1.53	<5.02	<1.71	<0.24	<0.31	<0.62	<0.40
M 2-9	<0.32	<3.55	<2.71	<15.0	<5.36	<1.53	<1.27	51.2 ± 2.08	51.6 ± 1.73	1.91 ± 0.12	1.96 ± 0.14	4.16 ± 0.16	3.86 ± 0.12
Mz 3 on	11.1 ± 0.54	32.5 ± 2.59	35.5 ± 1.59	19.8 ± 1.68	15.7 ± 2.39	7.10 ± 0.82	6.99 ± 0.46	21.5 ± 1.88	21.7 ± 0.67	0.67 ± 0.09	0.87 ± 0.11	15.2 ± 0.45	16.2 ± 0.20
Mz 3 off	4.50 ± 0.37	<3.98	<1.13	<8.60	<5.26	3.44 ± 0.90	2.16 ± 0.63	<4.77	5.64 ± 0.32	<0.28	<0.42	20.2 ± 0.38	20.4 ± 0.30
Mz 3 on-off	6.30 ± 0.37	33.0 ± 2.75	34.2 ± 1.65	17.5 ± 2.75	11.7 ± 2.65	4.65 ± 1.18	5.13 ± 0.67	17.8 ± 2.65	15.9 ± 0.70	0.68 ± 0.13	0.68 ± 0.16	<1.00	<0.55
NGC 40 on	3.21 ± 0.13	17.1 ± 0.87	18.5 ± 0.93	23.1 ± 7.29	19.3 ± 2.28	11.7 ± 0.91	11.9 ± 0.98	24.2 ± 1.42	22.1 ± 0.87	0.72 ± 0.08	0.69 ± 0.11	8.54 ± 0.19	9.55 ± 0.22
NGC 40 off	<0.17	<3.02	<1.90	<8.24	<3.57	<1.77	<0.97	<2.25	<0.84	<0.13	<0.20	0.50 ± 0.10	0.43 ± 0.09
NGC 40 on-off	3.17 ± 0.14	16.6 ± 1.53	16.7 ± 1.25	<18.2	19.7 ± 2.73	11.9 ± 1.25	11.9 ± 1.02	23.6 ± 1.69	21.6 ± 1.00	0.77 ± 0.08	0.70 ± 0.15	7.45 ± 0.20	8.77 ± 0.21
NGC 2346	0.97 ± 0.07	11.3 ± 0.64	10.9 ± 0.33	22.9 ± 2.08	23.4 ± 1.32	25.4 ± 0.86	24.3 ± 0.75	8.11 ± 0.96	8.25 ± 0.49	0.26 ± 0.04	0.33 ± 0.06	2.69 ± 0.11	2.93 ± 0.10
NGC 3132	3.79 ± 0.20	60.5 ± 2.01	65.9 ± 2.63	156. ± 5.53	156. ± 5.84	110. ± 3.19	111. ± 3.49	40.7 ± 1.39	41.1 ± 1.10	1.11 ± 0.08	1.31 ± 0.11	4.78 ± 0.14	5.52 ± 0.18
NGC 3242	<0.19	34.3 ± 2.43	29.7 ± 1.36	354. ± 11.8	338. ± 13.6	158. ± 4.49	153. ± 4.11	<3.27	<0.91	<0.18	<0.20	<0.23	<0.18
NGC 3918 on	0.32 ± 0.12	31.4 ± 1.93	31.7 ± 1.83	202. ± 7.75	200. ± 9.61	62.8 ± 2.58	63.0 ± 2.91	15.3 ± 1.44	16.0 ± 0.91	0.55 ± 0.07	0.60 ± 0.13	1.39 ± 0.10	1.56 ± 0.09
NGC 3918 off	<0.17	<2.76	<1.19	<7.71	<3.12	<1.78	<1.05	<2.35	<0.89	<0.18	<0.16	1.09 ± 0.13	1.14 ± 0.07
NGC 3918 on-off	<0.33	30.7 ± 2.20	31.3 ± 1.88	206. ± 9.39	201. ± 9.47	61.8 ± 2.85	63.4 ± 2.98	15.1 ± 1.77	15.5 ± 1.03	0.54 ± 0.07	<0.36	0.52 ± 0.14	0.45 ± 0.11
NGC 5189 on	1.59 ± 0.12	61.8 ± 1.73	67.9 ± 1.63	99.9 ± 5.55	99.6 ± 3.80	91.7 ± 2.20	84.9 ± 1.46	8.60 ± 2.17	8.53 ± 0.44	0.23 ± 0.06	0.31 ± 0.12	2.51 ± 0.11	3.08 ± 0.11
NGC 5189 off	<0.26	<4.36	<1.70	<16.8	<4.58	<2.31	<1.37	<3.62	1.69 ± 0.74	<0.20	<0.23	1.95 ± 0.12	2.70 ± 0.13
NGC 5189 on-off	1.26 ± 0.13	61.7 ± 2.17	67.9 ± 2.19	91.0 ± 9.30	99.5 ± 7.48	92.4 ± 2.47	84.5 ± 1.58	<5.85	6.52 ± 0.88	0.19 ± 0.05	0.26 ± 0.06	0.54 ± 0.08	0.34 ± 0.12
NGC 5315 on	0.73 ± 0.17	16.8 ± 1.88	17.4 ± 1.11	59.1 ± 5.42	50.7 ± 2.10	12.7 ± 0.88	11.8 ± 0.90	44.9 ± 1.94	47.9 ± 1.79	1.03 ± 0.08	1.38 ± 0.08	2.73 ± 0.07	3.22 ± 0.09
NGC 5315 off	<0.27	<2.30	<2.09	<5.57	<2.96	<2.03	<1.11	<2.05	<0.84	<0.19	<0.18	1.89 ± 0.23	1.45 ± 0.07
NGC 5315 on-off	0.60 ± 0.15	15.8 ± 2.22	18.3 ± 1.25	59.9 ± 7.27	49.8 ± 2.36	11.9 ± 1.38	11.4 ± 1.18	44.9 ± 2.23	47.3 ± 1.76	0.67 ± 0.10	1.40 ± 0.11	1.17 ± 0.12	1.78 ± 0.10
NGC 5882		29.4 ± 1.97			171. ± 6.53		58.8 ± 2.45						
NGC 6072 on	2.09 ± 0.15	28.0 ± 1.54	26.7 ± 0.89	62.7 ± 3.72	62.8 ± 2.56	53.5 ± 1.33	53.8 ± 1.22	20.8 ± 1.44	20.6 ± 0.54	0.87 ± 0.05	0.99 ± 0.11	5.40 ± 0.17	5.15 ± 0.09
NGC 6072 off	<0.18	<2.88	<1.32	<7.87	<3.79	<1.69	<0.91	<2.50	<0.84	<0.16	<0.20	1.15 ± 0.09	1.32 ± 0.08
NGC 6072 on-off	1.92 ± 0.16	28.0 ± 1.95	26.5 ± 1.01	64.2 ± 5.26	63.5 ± 2.84	53.1 ± 1.43	54.0 ± 1.34	20.5 ± 1.49	20.1 ± 0.60	0.83 ± 0.07	0.99 ± 0.17	4.24 ± 0.19	3.82 ± 0.12
NGC 6153 on	0.52 ± 0.15	147. ± 5.44	141. ± 6.88	529. ± 13.7	574. ± 23.7	164. ± 6.08	166. ± 5.36	<3.62	3.81 ± 0.49	<0.23	<0.21	3.74 ± 0.17	4.01 ± 0.11
NGC 6153 off	0.59 ± 0.13	<4.93	<1.07	<6.29	<5.26	<1.23	<0.89	<3.46	1.76 ± 0.18	<0.14	<0.21	4.49 ± 0.14	4.97 ± 0.13
NGC 6153 on-off	<0.31	147. ± 5.35	141. ± 6.87	528. ± 14.2	573. ± 23.7	164. ± 6.03	165. ± 5.28	<5.04	2.19 ± 0.56	<0.27	<0.27	<0.55	<0.38
NGC 6302 on	9.09 ± 0.56	164. ± 6.26	169. ± 5.73	155. ± 6.60	158. ± 7.03	51.9 ± 1.41	46.3 ± 2.06	289. ± 10.5	286. ± 9.47	11.8 ± 0.52	12.1 ± 0.34	24.8 ± 0.98	28.1 ± 0.52

Table A1 – *continued*

Source	[N II] 122 μm	[N III] 57 μm		[O III] 52 μm		[O III] 88 μm		[O I] 63 μm		[O I] 146 μm		[C II] 157 μm	
	LW2	SW2	SW3	SW1	SW2	SW5	LW1	SW2	SW3	LW3	LW4	LW3	LW4
NGC 6302 off	<0.58	<3.09	<2.02	<11.2	<3.98	<1.59	<1.21	3.66 ± 1.15	3.83 ± 0.36	<0.37	<0.49	13.7 ± 0.58	14.4 ± 0.23
NGC 6302 on-off	7.50 ± 0.65	164. ± 6.30	170. ± 5.66	156. ± 7.46	159. ± 7.68	51.0 ± 1.73	46.1 ± 1.90	286. ± 10.5	282. ± 9.48	10.2 ± 0.42	10.7 ± 0.31	12.3 ± 0.94	14.0 ± 0.46
NGC 6543	<0.34	125. ± 4.83	128. ± 5.61	515. ± 17.1	507. ± 20.7	150. ± 4.97	148. ± 5.01	8.09 ± 1.76	4.47 ± 0.40	0.23 ± 0.04	<0.27	0.54 ± 0.13	0.40 ± 0.09
NGC 6537 on (R470)	4.10 ± 0.37	50.3 ± 2.17	51.9 ± 2.14	37.6 ± 12.5	45.8 ± 3.31	20.4 ± 0.91	18.5 ± 0.98	54.7 ± 2.27	47.8 ± 2.05	2.23 ± 0.22	3.33 ± 0.28	16.6 ± 1.47	17.7 ± 0.30
NGC 6537 on (R703)	3.40 ± 0.50	42.0 ± 1.74	45.9 ± 2.57	41.0 ± 7.86	40.0 ± 2.14	14.4 ± 1.35	18.3 ± 0.99	46.7 ± 1.98	45.8 ± 2.07	2.44 ± 0.21	2.50 ± 0.21	15.4 ± 0.33	16.4 ± 0.43
NGC 6537 on (av)	3.24 ± 0.49	47.6 ± 1.54	47.7 ± 1.55	42.1 ± 9.08	40.8 ± 1.61	16.0 ± 0.95	19.6 ± 0.80	49.0 ± 1.30	47.2 ± 1.36	2.61 ± 0.19	2.41 ± 0.26	15.6 ± 0.47	16.9 ± 0.36
NGC 6537 off (R470)	<0.59	<2.67	<1.60	<6.28	<3.88	<1.55	<1.35	3.64 ± 1.46	3.43 ± 0.29	<0.62	<0.71	13.5 ± 0.40	14.0 ± 0.42
NGC 6537 on-off (R470)	2.90 ± 0.35	51.2 ± 2.33	52.1 ± 2.03	47.3 ± 12.7	47.3 ± 4.46	19.5 ± 1.07	16.4 ± 1.01	50.8 ± 2.53	44.6 ± 2.09	2.07 ± 0.34	3.09 ± 0.28	3.74 ± 0.35	3.58 ± 0.32
NGC 6537 on-off (R703)	2.22 ± 0.34	43.4 ± 2.03	45.9 ± 2.52	35.1 ± 6.19	40.5 ± 2.19	13.3 ± 1.63	16.4 ± 1.08	42.0 ± 2.32	42.5 ± 2.04	1.78 ± 0.20	1.95 ± 0.33	1.38 ± 0.25	2.33 ± 0.26
NGC 6537 on-off (av)	3.07 ± 0.26	49.1 ± 1.73	47.9 ± 1.42	37.0 ± 7.57	41.4 ± 2.18	14.9 ± 1.17	17.5 ± 0.84	45.0 ± 1.84	43.9 ± 1.35	1.87 ± 0.19	2.29 ± 0.23	1.75 ± 0.52	2.43 ± 0.24
NGC 6567		<3.30			34.8 ± 2.77		8.31 ± 0.62						
NGC6572 on	<0.17	24.1 ± 2.72	22.7 ± 1.39	169. ± 7.60	151. ± 7.33	24.7 ± 1.20	24.7 ± 1.16	51.9 ± 2.69	47.3 ± 2.06	1.12 ± 0.07	1.17 ± 0.18	2.34 ± 0.14	2.59 ± 0.14
NGC6572 off	<0.18	<2.30	<0.93	<10.4	<3.47	<1.45	<0.85	<2.55	<1.00	<0.12	<0.25	0.30 ± 0.05	0.39 ± 0.07
NGC6572 on-off	<0.26	22.5 ± 3.30	23.8 ± 1.25	163. ± 9.97	151. ± 7.29	24.8 ± 1.32	25.5 ± 1.15	53.0 ± 3.11	47.4 ± 1.99	1.20 ± 0.10	1.04 ± 0.18	2.06 ± 0.15	2.21 ± 0.15
NGC 6578		30.6 ± 2.75			135. ± 6.11		43.5 ± 1.95						
NGC 6720	3.93 ± 0.19	83.9 ± 2.55	77.9 ± 2.22	249. ± 8.28	268. ± 5.58	188. ± 3.78	183. ± 2.71	60.4 ± 1.93	57.6 ± 0.89	1.77 ± 0.09	1.93 ± 0.13	6.45 ± 0.26	7.30 ± 0.28
NGC 6741		6.69 ± 2.88			25.7 ± 2.48		5.45 ± 0.45						
NGC 6781 on	3.33 ± 0.22	55.3 ± 1.82	58.6 ± 0.83	147. ± 2.65	152. ± 2.62	143. ± 1.48	131. ± 2.34	27.1 ± 1.12	26.3 ± 0.49	0.88 ± 0.13	1.44 ± 0.13	7.41 ± 0.22	7.91 ± 0.34
NGC 6781 off	<0.23	<2.25	<1.48	<7.77	<3.56	<1.62	<1.14	<3.16	0.79 ± 0.29	<0.13	<0.28	1.40 ± 0.08	1.51 ± 0.09
NGC 6781 on-off	3.02 ± 0.24	54.4 ± 2.59	58.7 ± 1.10	149. ± 5.54	152. ± 2.95	143. ± 1.40	131. ± 2.29	26.5 ± 1.80	25.4 ± 0.56	0.95 ± 0.11	1.02 ± 0.13	5.99 ± 0.20	6.52 ± 0.37
NGC 6790		<3.25			11.7 ± 2.34		<1.66						
NGC 6826	<0.19	37.3 ± 2.02	38.0 ± 1.57	201. ± 6.60	210. ± 9.43	77.0 ± 2.70	79.7 ± 2.98	<5.39	<1.34	<0.15	<0.21	<0.20	0.32 ± 0.07
NGC 6884		9.13 ± 1.72			57.3 ± 3.32		17.2 ± 0.90						
NGC 6886		<2.67			14.6 ± 1.71		2.97 ± 0.43						
NGC 7009	<0.24	56.9 ± 2.62	57.6 ± 2.65	386. ± 14.8	393. ± 18.0	131. ± 3.96	127. ± 4.19	<3.10	<1.07	<0.11	<0.35	<0.25	<0.23
NGC 7662	<0.28	20.1 ± 1.91	18.3 ± 0.77	216. ± 9.47	196. ± 8.86	76.9 ± 2.64	79.6 ± 2.57	<2.60	<0.66	<0.17	<0.17	<0.25	0.18 ± 0.08
Vy 2-2 on	<0.26	<2.64	<1.61	<12.8	<5.10	<2.00	<1.03	8.97 ± 1.75	9.27 ± 0.49	0.31 ± 0.08	<0.32	1.63 ± 0.15	2.21 ± 0.09
Vy 2-2 off	<0.43	<2.30	<1.56	<9.82	<4.57	<2.02	<1.05	<3.17	<0.81	<0.22	<0.42	1.28 ± 0.19	1.34 ± 0.10
Vy 2-2 on-off	<0.36	<3.76	<2.25	<16.4	<7.09	<2.95	<1.66	8.06 ± 1.53	8.36 ± 0.66	<0.29	<0.57	<0.70	0.96 ± 0.15

Note: R079, R699, etc., are *ISO* orbit numbers during which the observations were carried out.

This paper has been typeset from a TEX/LATEX file prepared by the author.